

# A full-scale clinical prototype for proton range verification using prompt gamma-ray spectroscopy

**Fernando Hueso-González<sup>1</sup>, Moritz Rabe<sup>1</sup>, Thomas A Ruggieri<sup>1</sup>,  
Thomas Bortfeld<sup>1</sup>, Joost M Verburg<sup>1</sup>**

<sup>1</sup>Massachusetts General Hospital and Harvard Medical School, Department of Radiation Oncology, Boston, MA 02114, USA

E-mail: [jverburg@mgh.harvard.edu](mailto:jverburg@mgh.harvard.edu)

**Abstract.** We present a full-scale clinical prototype system for in vivo range verification of proton pencil-beams using the prompt gamma-ray spectroscopy method. The detection system consists of eight LaBr<sub>3</sub> scintillators and a tungsten collimator, mounted on a rotating frame. Custom electronics and calibration algorithms have been developed for the measurement of energy- and time-resolved gamma-ray spectra during proton irradiation at a clinical dose rate. Using experimentally determined nuclear reaction cross sections and a GPU-accelerated Monte Carlo simulation, a detailed model of the expected gamma-ray emissions is created for each individual pencil-beam. The absolute range of the proton pencil-beams is determined by minimizing the discrepancy between the measurement and this model, leaving the absolute range of the beam and the elemental concentrations of the irradiated matter as free parameters. The system was characterized in a clinical-like situation by irradiating different phantoms with a scanning pencil-beam. A dose of 0.9 Gy was delivered to a  $5 \times 10 \times 10 \text{ cm}^3$  target with a beam current of 2 nA incident on the phantom. Different range shifters and materials were used to test the robustness of the verification method and to calculate the accuracy of the detected range. The absolute proton range was determined for each spot of the distal energy layer with a mean statistical precision of 1.1 mm at a 95% confidence level and a mean systematic deviation of 0.5 mm, when aggregating pencil-beam spots within a cylindrical region of 10 mm radius and 10 mm depth. Small range errors that we introduced were successfully detected and even large differences in the elemental composition do not affect the range verification accuracy. These results show that our system is suitable for range verification during patient treatments in our upcoming clinical study.

## 1. Introduction

The advantageous depth-dose deposition profile of protons cannot yet be fully utilized in clinical practice because of uncertainty in the beam range within the patient. The origin of this uncertainty is the determination of the stopping power of tissue along the beam path, which is affected by the CT imaging, the degeneracy in the conversion from x-ray attenuation to stopping power, and the uncertainty in the ionization potential of human tissue (Andreo 2009). Furthermore, interfractional and intrafractional patient positioning errors and anatomical changes can affect the range. Conservative safety margins (Albertini et al. 2011) and robust treatment planning (Unkelbach et al. 2007) are currently required to ensure a complete tumor coverage.

Efforts are being undertaken to reduce proton range uncertainty and the required safety margins by performing an *in vivo* verification of the range during patient treatment. Several methods have been suggested (Knopf et al. 2013), but no solution is available for routine clinical use. The use of prompt gamma-rays, which originate from proton-nuclear interactions with tissue, was proposed by Jongen et al. (2003) and is being actively investigated by various groups (Krimmer et al. 2018). The virtually instantaneous emission of the gamma-rays, with a time scale smaller than  $10^{-11}$  s, enables real-time range verification of the delivered proton pencil-beams. Through the high gamma-ray energy of typically several MeV, most of them escape the patient and can be detected externally. For a successful clinical application, a detection system has to meet several requirements. It needs to detect a sufficient number of gamma-rays during a fractionated clinical treatment with fields that deliver a dose on the order of 1 Gy to the tumor, such that the range can be determined with millimeter precision. The correlation of the measured gamma-ray emissions with the proton dose deposition needs to be accurately known to minimize systematic bias. Determining this correlation based on first principles requires extensive modeling of the nuclear reactions (Verburg et al. 2014), but more empirical methods are also being investigated (Schumann et al. 2016). To not extend the duration of the treatments, the detection needs to be performed while the protons are delivered at a standard clinical beam current of about 2 nA incident on the patient. Under these conditions and with a sufficiently efficient system, a detector load of millions of gamma-rays per second is expected. The detection system also needs to function stably under the highly variable count rates that occur during proton pencil-beam delivery. These are certainly challenging requirements.

Individual prompt gamma-rays can be detected with scintillation detectors (Seo et al. 2006; Smeets et al. 2012; Pinto et al. 2014; Krimmer et al. 2017; Pausch et al. 2016; Verburg et al. 2013), which need to be dense and thick to absorb the full energy. A form of collimation is needed to reconstruct the spatial origin of the emission. Collimation is only needed along the depth dimension, because the lateral position of each incident pencil-beam is monitored with an ionization chamber in the beam line. A physical collimator made of a high-Z material, with one or multiple slits perpendicular to the proton beam direction, limits the longitudinal position along the beam path from where the detected gamma-rays originate. Another advantage of a physical collimator is the shielding of gamma-rays emitted in the beam entrance path, which

do not provide valuable information about the proton range. Alternatively, the transit time of the protons in tissue until the prompt gamma-ray is emitted can be used as a form of virtual collimation (Golnik et al. 2014; Hueso-González et al. 2015). Such time-based collimation reduces weight and adds geometric flexibility. However, because of the time spread of the incident protons in a bunch from a clinical proton acceleration system (Petzoldt et al. 2016), the origin of the gamma-ray emission is less well defined than for passive collimation. It also adds uncertainty because of the need to correlate the proton transit time with a spatial location in the patient. Finally, the application of Compton cameras is being investigated (Hueso-González et al. 2017; Solevi et al. 2016; Aldawood et al. 2017; Rohling et al. 2017; Draeger et al. 2018). These systems do not require physical collimation either, but rely on the detection of multiple Compton scatter interactions per incident gamma-ray in order to reconstruct its origin region.

Prompt gamma-ray imaging is an indirect range verification method that exploits the correlation of the nuclear reaction positions with the deposited dose. Nuclear interactions between accelerated protons and the nuclei of human tissue are complex processes. Numerous nuclear reaction channels of protons with the main nuclei of tissue,  $^{12}\text{C}$  and  $^{16}\text{O}$ , exist. The residual nuclei de-excite through the emission of gamma-rays with different discrete energies. The patient-specific emissions of prompt gamma-rays during the treatment can be modeled based on the CT scan, the treatment plan and nuclear physics models. Matching this model with the measured prompt gamma-ray distribution provides a means to verify the ranges of the proton pencil-beams.

In this context, it is important to define the goal of the range verification method. One approach is to detect a deviation in the beam range through the comparison of measurements from different treatment days. Such a detection would be clinically useful for quality assurance, to verify the consistency among the delivered fractions. However, this approach does not provide an estimate of the absolute proton range. Reducing the initial range margins, which is our goal, imposes a more difficult requirement on the range verification. It requires an accurate and robust determination of the absolute range of the beam with only the treatment plan as prior knowledge.

Recently, initial studies of prompt gamma-ray detection during patient treatments with passively scattered protons (Richter et al. 2016) and actively scanned proton pencil-beams (Xie et al. 2017) were performed with a scintillation detector array combined with a knife-edge slit collimator. Xie et al. (2017) measured the integral number of prompt gamma-rays during the pencil-beam delivery. The median statistical precision of the range verification for a set of distal layers was  $\pm 12$  mm at 95% confidence ( $2\sigma$ ) for individual pencil-beams, and  $\pm 4.2$  mm after aggregating pencil-beams laterally within the same layer with a Gaussian kernel with a 7 mm standard deviation. The positioning accuracy of the setup was estimated as  $\pm 1.5$  mm at  $2\sigma$  (Xie et al. 2017). The bias in the absolute range from sources other than positioning was not discussed. In the case of Compton cameras, relative range shifts of a few millimeters are theorized to be detectable with larger scale Compton camera systems (Draeger et al. 2018), which have not been constructed yet.

For several years, we have been developing a proton range verification method that is uniquely based on prompt gamma-ray spectroscopy (Verburg et al. 2013; Verburg et al. 2012;

Verburg et al. 2014). This method uses both the arrival time and energy of the detected prompt gamma-rays. Using a small-scale prototype, we first showed energy- and time-resolved prompt gamma-ray spectra that were measured during the delivery of proton beams (Verburg et al. 2013). We use detailed models of the nuclear reactions associated with the discrete prompt gamma-ray emissions to verify the absolute range of proton beams in phantoms, without requiring prior knowledge of the elemental composition of the irradiated matter (Verburg et al. 2014). Moreover, the measurement of the arrival time of the gamma-rays allows a separation of proton- and neutron-induced gamma-rays, which removes the confounding uncertainty from the neutron-induced gamma radiation background in the treatment room.

In this paper, we describe the development and evaluation of a new full-scale clinical prototype detection system for proton range verification based on prompt gamma-ray spectroscopy. This system will be deployed for the first clinical study with patients. We present the detectors, collimator and data processing methods in section §2. Section §3 describes a fully integrated clinical workflow for modeling the prompt gamma-ray emissions based on the treatment plan, in order to predict the number of gamma-rays detected when different range errors occur, and to verify the proton range by comparing the measurements with the model. The experimental setups that we use to optimize the cross section data and to evaluate the range verification performance of the system are shown in section §4. The results of the experiments are given in section §5, in which we assess the detector performance and the accuracy and statistical precision of the proton range verification. In section §6, we discuss the obtained results and the consequences for the clinical implementation, and the main conclusions of the study are drawn in section §7.

## **2. Detectors and data processing**

### *2.1. Proton beam*

The experiments were performed in the pencil-beam scanning treatment gantry at the Francis H. Burr Proton Therapy Center, Massachusetts General Hospital. Protons were accelerated to 230 MeV with an IBA C230 cyclotron (Ion Beam Applications SA, Louvain-la-Neuve, Belgium), degraded by an energy selection system, and transported to the treatment room along a beam line with a length of approximately 35 meters. The cyclotron features a radiofrequency of 106.3 MHz. All pencil-beam layers were delivered with the standard clinical system at the full beam current of 2 nA incident on the phantom, which corresponds to a bunch of approximately 100 protons every 9.4 ns. Based on routine quality assurance measurements, the reproducibility of the beam range in water is known to be better than 0.5 mm.

### *2.2. Detectors and collimator*

Gamma-rays are detected using eight detector modules, each consisting of a cerium-doped lanthanum(III) bromide scintillation crystal (Saint-Gobain, Saint Pierre Lès Nemours, France) with a diameter of 50.8 mm and a length of 76.2 mm, a photomultiplier tube, and a custom base with a Cockcroft–Walton high voltage generator and a transistorized voltage divider. The

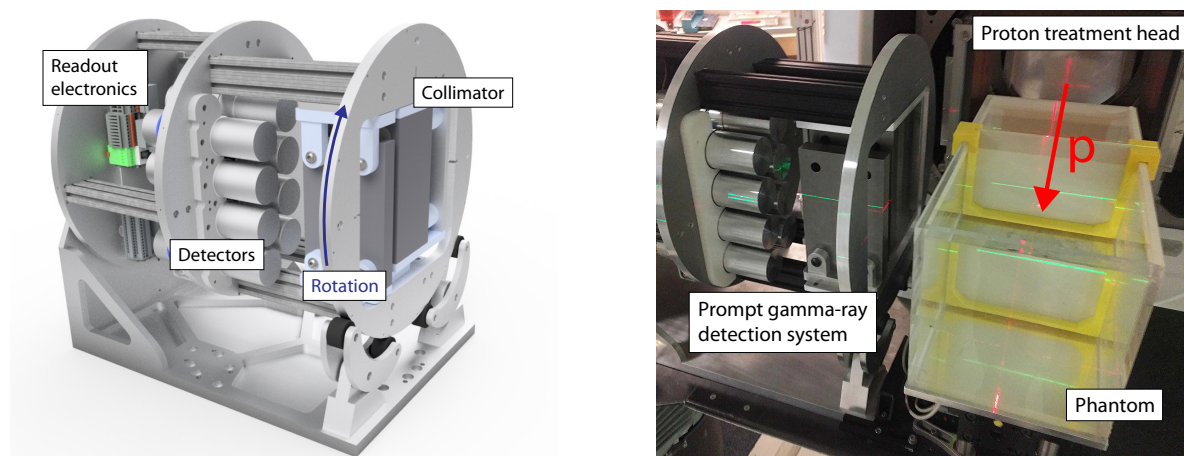


**Figure 1:** Left: 3D model of the clinical prototype system, which can rotate around its axis according to the beam incidence angle. The tungsten collimator is visible on the front plane, the eight scintillation detectors in the middle and the readout electronics on the back plate. Right: photo of the system in the gantry treatment room. The red arrow shows the proton beam incidence direction.

total volume of scintillation material is  $1236 \text{ cm}^3$ . The detector signals from the anode of the photomultipliers are amplified with transimpedance amplifiers that are located next to the detectors. The scintillators and electronics are designed to sustain high overall event rates of up to  $10^7$  events per second.

The gamma-rays in the entrance path of the beam are shielded by a 127 mm thick and 102 mm wide block of tungsten. Along the beam direction, this is followed by a slit opening of 12.7 mm and a single collimator slab with a width of 25.4 mm. Four detectors are stacked with their center aligned with the edge of the proximal collimator. The other four detector modules are located distal of these detectors in a closely packed configuration (see figure 1). Each row of detectors therefore focuses on a different position along the beam direction. Because many of the prompt gamma-rays interact through Compton scattering or pair production, the volume of scintillation material that is not directly in view of the primary prompt gamma-rays contributes to the probability of the absorption of the full photon energy.

### 2.3. Data acquisition system

The detectors are connected to a custom data acquisition system located in the treatment control room. This system is synchronized with the pencil-beam delivery system and the cyclotron. The signals from the eight detector modules are independently read out with a 14-bit analog-to-digital converter that is phase-locked to the accelerator at a frequency of twice the cyclotron radiofrequency, resulting in a sample rate of approximately  $2.13 \times 10^8$  samples per second. The data from the analog-to-digital converters are processed in real-time by field-programmable-gate arrays (FPGAs). A trigger to acquire an event is generated when the digitized signal magnitude exceeds a predefined threshold.

The gamma-ray energy is calculated by integrating the area under the pulse signal over a time window of 200 ns. The pulse shape is used to determine whether the gamma-ray event is a single gamma-ray detection or a pile-up of several gamma-rays (section §2.6). The calculations and the storage in memory result in a dead-time of 150 ns after each event, during which the individual detector module is not sensitive to a new event. Because of the fast detectors and the short dead-time, the average separation time between two gamma-ray events is much longer than the time required to acquire an event. We can typically acquire about 90% of the gamma-rays that interact with the detectors and deposit an energy within the range of interest.

To find the precise arrival time of the gamma-ray, we subtract a delayed copy of the digital signal from the original one and find the zero crossing time of the resulting signal. This time point is independent of the signal magnitude. The arrival time analysis is first performed with a time resolution equal to the sample rate. Subsequently, we use a polynomial interpolation to achieve sub-nanosecond resolution.

A second data acquisition board performs real-time acquisition of the pencil-beam delivery status and the signals from the beam monitoring electronics. It also enables the detector readout only during the beam-on periods. The clock of this board is synchronized with the detector readout board, therefore providing the exact beam status of the pencil-beam delivery for each detected gamma-ray.

The acquired data are stored in a memory buffer that is continuously read out by the control software, which is a custom C++ application on a Linux system. This application provides a real-time graphical display of the acquired data and the beam status. An important task of this software is to perform various corrections to normalize all measurements to absolute units, independently of conditions such as the detector load and the neutron-induced background, as will be discussed in the next sections.

#### 2.4. Energy calibration

Although the detector readout electronics are designed for high stability at various detector count rates, a small dependency of the signal amplitude as a function of the count rate is unavoidable. Moreover, any scintillator has some temperature dependence. To make the measurements independent of these factors, an automated energy calibration as a function of the detector count rate is implemented. After applying the initial fixed calibration factor, an energy correction function is determined for each proton energy layer using the gamma-rays from neutron capture by hydrogen at 2.22 MeV, which are very abundant in every measurement. A 2D histogram with the uncorrected line energy as a function of the pencil-beams ordered by count rate is created. A 2D curve is fitted, namely a normal distribution in the energy dimension with a shifting mean value, which is linearly correlated to the ordered pencil-beam number. The benefit of simultaneously considering all pencil-beams within a layer is that statistical variations have negligible impact. The ratio between the uncorrected energy at the peak position and the actual gamma-ray energy of the neutron-hydrogen line is applied as a small correction on the order of 1%.

A very small non-linearity is also present in the correlation of the signal amplitude with energy. The correction for this effect is also automated and is the same for all pencil-beams. This correction is performed by analyzing the spectral position of a few strong gamma-ray lines with known energies and fitting a polynomial correction function, which is then applied to all measurements.

### 2.5. Time calibration

The gamma-ray arrival time relative to the cyclotron radiofrequency period is different for each energy layer because of the different flight times of the protons through the beam lines. For each detector and spot, we automatically center the proton-induced prompt gamma-ray peak in the time dimension. Due to space charge effects in the photomultiplier, the shape of the detector signals slightly depends on the energy. To remove any energy dependency in the arrival time, a correction is applied by finding the location of the proton-induced peak in the time dimension for several energy regions and by performing a linear fit. This is similar to the method described by Hueso-González et al. (2014).

### 2.6. Pile-up rejection

Piled-up events, where multiple gamma-rays interact with the detector at almost the same time such that they can not be separated, are detected using pulse shape analysis. A set of expected pulse shape parameters and their variance were obtained from a laboratory measurement at a very low event rate. Whenever one parameter is outside the expected nominal window, i.e., the regular pulse shape, the event is marked as a piled-up event and discarded from further analysis. The acceptance window is calibrated for each detector separately to account for the slight differences in pulse shape between detectors.

A small fraction of the piled-up events cannot be detected by this method. This can happen if two events are very close to each other in time ( $T_1 = 15$  ns) so that the sum of pulse shapes is similar to a single one, independently of their respective energies; or if the second event arrives within  $T_2 = 150$  ns, but has a small energy with respect to the previous one, so that the pulse shape difference is not significant. Consequently, events with a wrong energy or time stamp are included in the analysis as valid events, but contribute to the background rather than to resolved lines. A correction scale factor  $S$  is applied depending on the detector count rate  $R$ :

$$S = \exp[R(f_1 \times T_1 + f_2 \times T_2)], \quad (1)$$

in which  $f_1$  and  $f_2$  are empirically determined parameters for the two aforementioned effects and  $T_1$  and  $T_2$  are the corresponding time constants. The values of these parameters are determined such that the magnitude of the proton-induced gamma-rays acquired in a fixed time period is proportional to the proton beam current.

### 2.7. True number of events

The number of valid events  $N_E$  during the delivery of a pencil-beam is lower than the true number of events  $N_T$  because of the dead-time and pile-up of two or more gamma-rays. To

determine the true number of events, we take advantage of the fact that Poisson statistics apply to the occurrence of the events. This assumption is valid if the dose rate is constant, which is a good approximation because the duration of the pencil-beam delivery is much longer than the duration of the ramp-up and ramp-down processes. As described by Bécaries et al. (2012), Poisson statistics imply that the separation times between consecutive events feature an exponential distribution. We fit the measured separation time distribution for times that exceed the pulse duration and dead-time. The true number of events is then given by the integral of the fitted distribution, including also the virtual events with a short separation time that precluded them from being acquired. The correction is applied as a scaling factor  $D = N_T/N_E$  equal to the ratio between true and acquired events.

### 2.8. Coincidence rejection

When analyzing discrete gamma-ray lines, it is desirable to reject events in which Compton scatter occurred in the scintillator. In these events, the full energy of the gamma-ray was not absorbed in a single detector and therefore the event contributes only to the continuum background. If the scattered gamma-ray interacts with a second detector, we are able to reject such events through the analysis of coincidences between the detectors. If events in separate detectors are separated in time by less than 3 ns, both events are rejected.

There is a small probability of erroneously rejecting events that are not due to Compton scatter. This is corrected for each pencil-beam by using a random coincidence correction, based on a histogram of the time difference between consecutive events in different detectors. It is expected to present a baseline plus a peak of true coincidences around zero. The total number of coincidences  $N_C$  is the integral of the histogram within the coincidence window. The number of random coincidences  $N_R$  is determined by fitting the baseline of the histogram with a quadratic curve and calculating its integral within the aforementioned window. The random coincidence correction  $C$  is calculated as:

$$C = 1 + \frac{1/N_E}{1/N_R - 1/N_C}. \quad (2)$$

### 2.9. Histogram analysis

The fully corrected data are combined in 2D histograms with dimensions of energy and time (Verburg et al. 2013). We create two histograms for each proton pencil-beam: one for each row of four detectors, see figure 1. An iterative method is used to split the measured 2D histograms into three different components:

**Proton-induced continuum.** Prompt gamma-rays that undergo incoherent scattering in the detector, or that have scattered before reaching the detector, contribute to an unresolved background in the energy dimension, but are well resolved in the time dimension. A second contribution to the unresolved continuum is from a quasi-continuum of discrete gamma-rays from the cascade decay of higher excited states (Capote et al. 2009), which cannot be resolved as separate lines.

**Neutron-induced continuum.** Like the proton-induced continuum, the neutron-induced gamma-rays can also scatter before or inside the detector, or stem from unresolved cascades. This structure is both unresolved in time and energy.

**Resolved lines.** Subtracting the continuum components results in a histogram with only resolved lines. They correspond to prompt gamma-rays that either deposit the full energy in one of the detectors, or the full energy minus one or two 511 keV escape photons. These peaks are resolved in both the energy and time dimension. In addition, neutron-induced reactions such as the neutron capture of hydrogen result in lines that are resolved in energy but not strongly resolved in time.

A robust separation of these three components is crucial, because it allows a direct comparison of the measurements with fundamental physics models. The discrete proton-induced gamma-ray lines can be fully modeled based on nuclear reaction cross sections, and their quantification also carries the essential information about the elemental concentrations in the irradiated tissue. For a spot-wise 2D separation of proton- and neutron-induced events, a dedicated algorithm was designed: the Recursive Bisection Neutron Subtraction (ReBiNS). First, a time projection of the 2D histogram is obtained for all energy bins. The neutron background is estimated on the resulting 1D time spectrum  $M(t)$  by means of the SNIP algorithm (Ryan et al. 1988). The proton-induced histogram is obtained by subtracting the neutron background from the original histogram  $M(t)$ . Both the neutron-induced and proton-induced 1D histograms are normalized and fitted by cubic splines, serving as numeric probability density functions of the neutron  $s_n(t)$  and proton  $s_p(t)$  time structures. Then, the time spectrum  $M(t)$  is fitted to

$$M(t) = N \times s_n(t) + P \times s_p(t), \quad (3)$$

where  $N$  is the number of neutron-induced counts,  $P$  the number of proton-induced counts, and  $N + P$  is constrained to the total number of histogram entries  $T$  in  $M$ . Once the parameters are calculated, a similar fit is done for each energy bin individually. To ensure the robustness and consistency with the global fit, a recursive bisection strategy is applied. First, two time projections  $a$  and  $b$  are created among the upper and lower half of the 2D energy-over-time spectrum. Then, a simultaneous fit of equation (3) is done on both projections, but with fixed shapes  $s_n(t)$ ,  $s_p(t)$  and the cross-constraints  $N_a + N_b = N$ ,  $P_a + P_b = P$ ,  $N_a + P_a = T_a$ ,  $N_b + P_b = T_b$ . Each of the regions is again divided in two sub-regions, and the procedure is repeated recursively until the sub-regions consist of single energy bins  $i$ . The set of fitted parameters  $N_i$  and  $P_i$  can be interpreted as an energy spectrum of the neutron-induced and proton-induced contributions. Both 1D spectra are further analyzed to separate the continuum background from the resolved lines by means of the SNIP algorithm.

The magnitude of the gamma-ray lines is determined by a 2D fit of the resolved line histogram. The peaks are modeled as Gaussians in the energy dimension and as  $s_p(t)$  in the time dimension, or  $s_n(t)$  in the case of resolved neutron-induced lines.

### 2.10. Lateral spot merging

For range verification, we create histograms in which the data of neighboring pencil-beams within the same energy layer are summed if their center position is within a 10 mm lateral

**Table 1:** Indices used within the prompt gamma-ray emission and detection model.

Index	Bins	Step	Min.	Max.	Description
$v$	# voxels	1	0	# voxels	voxel of the field of view ( $120 \times 160 \times 160$ )
$p$	# pixels	1	0	# pixels	pixel of the front plane ( $120 \times 160$ )
$e$	150	1 MeV	0 MeV	150 MeV	proton kinetic energy within the field of view
$s$	# spots	1	0	# spots	spot of the treatment plan
$l$	7	1	0	6	prompt gamma-ray line (0: 1.6 MeV, 1: 2.0 MeV, 2: 2.3 MeV, 3: 2.8 MeV, 4: 4.4 MeV, 5: 5.2 MeV, 6: 6.1 MeV)
$t$	2	1	0	1	target nucleus (0: oxygen $^{16}\text{O}$ , 1: carbon $^{12}\text{C}$ )
$\theta$	360	$0.25^\circ$	$0^\circ$	$90^\circ$	polar angle
$\phi$	360	$1.00^\circ$	$0^\circ$	$360^\circ$	azimuthal angle
$a$	5	1	0	4	absorption process: (0) full, (1) single and (2) double escape, (3): any energy deposit between 1.4 MeV and 3.0 MeV, or (4): higher than 3.0 MeV.
$d$	8	1	0	7	scintillation detector
$r$	2	1	0	1	row of detectors (0 : $\sum_{d=0}^3$ , 1 : $\sum_{d=4}^7$ )
$c$	17	1	0	16	discrete range error scenario in steps of 1 mm ( $c = 8 \rightarrow$ nominal scenario)

radius of the spot under consideration. With our beam delivery system, this usually results in data from seven pencil-beams to be accumulated. Based on Poisson statistics, one would theoretically expect this to yield an improvement of the statistical precision by a factor of 2.6, at the expense of a reduction in spatial resolution. Note that considerable overlap already exists between neighboring pencil-beams near the end-of-range because of multiple Coulomb scattering.

### 3. Range verification method

A sophisticated simulation of the fundamental physical processes like nuclear interactions, attenuation and detector system response was developed to accurately predict the prompt gamma-ray emissions and detections. This model is compared to the measurement data to determine the proton range for each pencil-beam.

The model is split up into several parts: geometry definition, CT to material conversion, proton stopping process, prompt gamma-ray emission, gamma-ray attenuation, and detection. An overview of the indices and parameters defined in subsequent sections is presented in tables 1 and 2, and a graphical workflow is shown in figure 2.

#### 3.1. Field of view

A volume of 12 cm in the direction parallel to the proton beam path (x axis), 32 cm in the direction perpendicular to the pencil-beams pointing towards the detector system (z axis) and 32 cm in the third dimension (y axis) is defined as the field of view (FOV) of the detector, see

**Table 2:** Parameters used within the prompt gamma-ray emission and detection model.

Parameter	Description	Source
$m^v$	material composition in voxel $v$ .	CT, Schneider et al. (2000)
$\mu^{vl}$	attenuation coefficient in voxel $v$ in $\text{cm}^{-1}$ for a $\gamma$ -ray with energy $l$ .	$m$ , XCOM Berger et al. 2010
$\rho^{vt}$	concentration by mass of target $t$ in voxel $v$ in $\text{g}/\text{cm}^3$ . $\hat{\rho}^{vt}$ : expected, $\rho^{vt}$ : optimized.	CT
$N_p^{csve}$	protons in voxel $v$ with energy $e$ for spot $s$ and range error scenario $c$ .	GPU
$\sigma^{elt}$	differential cross section at 90 degrees of a proton with energy $e$ reacting with target $t$ and emitting a prompt $\gamma$ -ray with energy $l$ . $\hat{\sigma}^{elt}$ : expected, $\sigma^{elt}$ : optimized.	Verburg et al. (2014)
$\psi^{eta}$	effective cross section accounting for all prompt $\gamma$ -rays from unresolved energy levels $l > 6$ at target $t$ for absorption processes $a = 3, 4$ and proton energy $e$ .	Experiment
$\delta^v$	average intersection length of the proton beam track with voxel $v$ .	FOV grid, 1 mm
$N_\gamma^{cslvt}$	prompt $\gamma$ -rays of transition $l$ of nucleus $t$ emitted in voxel $v$ for spot $s$ and range error scenario $c$ .	$N_p \rho \sigma$
$\tau^{vl\theta\phi}$	probability that a prompt $\gamma$ -ray with energy $l$ emitted in voxel $v$ in direction $(\theta, \phi)$ reaches the front plane $z = 160$ mm without interaction.	$\mu$ , ray tracing
$\eta^{p\theta\phi l da}$	probability that a prompt $\gamma$ -ray with energy $l$ crossing the pixel $p$ of front plane $z = 160$ mm at an angle $(\theta, \phi)$ undergoes absorption process $a$ in detector $d$ .	TOPAS Perl et al. 2012
$\xi^{vl da}$	probability that a prompt $\gamma$ -ray with energy $l$ emitted in voxel $v$ reaches the front plane without undergoing any interaction and then undergoes absorption process $a$ in detector $d$ .	$\eta \tau$
$\zeta_\gamma^{csltda}$	expected number of prompt $\gamma$ -rays undergoing absorption process $a$ in detector $d$ , that were emitted from target nucleus $t$ and from transition $l$ for spot $s$ and range error scenario $c$ .	$N_\gamma \xi$
$C_\gamma^{slra}$	measured $\gamma$ -rays from transition $l$ , absorption process $a$ for spot $s$ and detector row $r$ .	Experiment
$k^{st}$	elemental concentration correction factor ( $\rho = k\hat{\rho}$ ) for target $t$ and spot $s$ .	Experiment, Fit
$\epsilon^s$	absolute range error for spot $s$ , namely the difference between the optimized and the planned range $\epsilon = (c - 8) \times (1 \text{ mm})$ .	Experiment, Fit

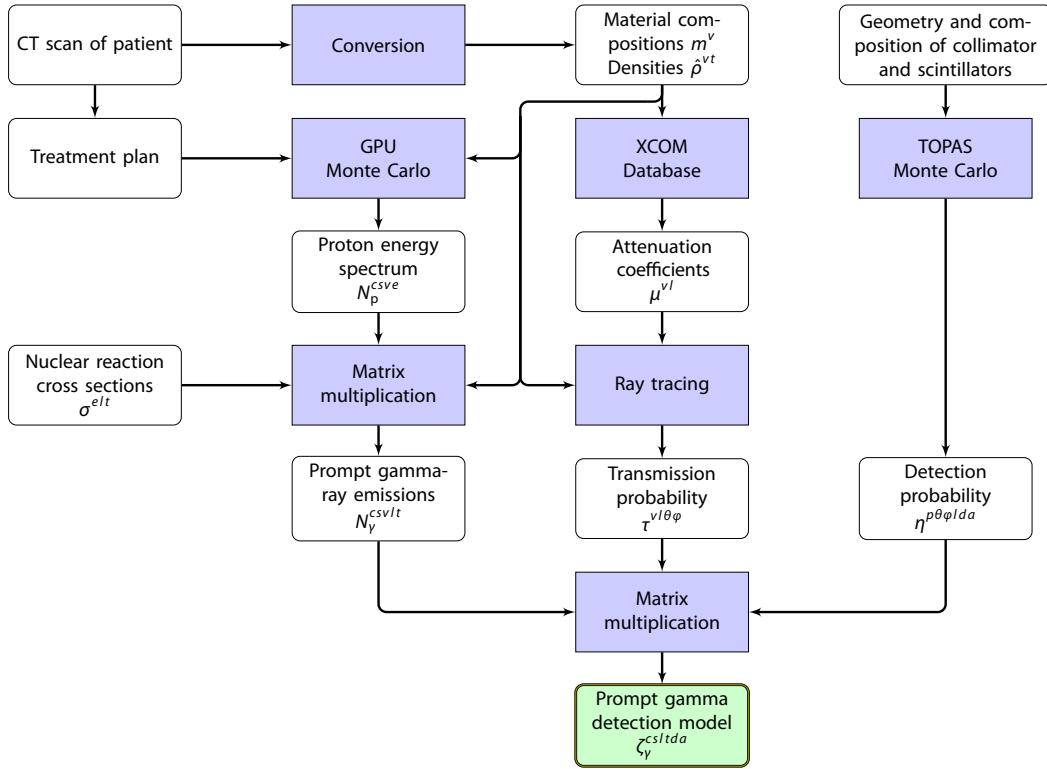


**Figure 2:** Simplified workflow chart visualizing the prompt gamma-ray detection model generation based on the CT scan of the patient, the treatment plan, the detector geometry, the tabulated nuclear cross sections and the XCOM database. GPU and TOPAS Monte Carlo simulations, as well as analytical ray tracing are performed. The mathematical symbols are described in table 2.

figure 3. This volume is discretized into voxels of  $1 \times 2 \times 2 \text{ mm}^3$  to define a grid on which the simulation is performed. The voxel size in the dimension parallel to the beam path is set to the smallest distance of 1 mm, since this axis corresponds to the direction along which the range verification is performed. The FOV therefore consists of  $120 \times 160 \times 160$  voxels. We define the front plane of the FOV at the surface  $z = 160 \text{ mm}$ , which is divided in  $120 \times 160$  pixels, as seen in figure 3.

### 3.2. CT scan and material conversion

As the first step of the model simulation, the CT numbers of the patient or phantom scan are interpolated onto the FOV grid. Based on standard conversion schemes, the following data are estimated for each voxel  $v$ : the material composition  $m^v$ , the mass concentration  $\hat{\rho}^{vt}$  of oxygen and carbon, and the attenuation coefficient  $\mu^{v/l}$  that depends on the gamma-ray line energy  $l$ . The material composition and density conversions needed for the simulation are retrieved from the CT scan using the conversion scheme of Schneider et al. 2000, whereas the attenuation coefficients are extracted from the XCOM database (Berger et al. 2010). These will be the input data for the next simulation steps. Note that the model relies to some extent on prior information of the initial CT scan, but can later be adjusted by leaving the oxygen and carbon concentrations as free parameters  $\rho^{vt}$ . The reason for focusing on those two elements is that

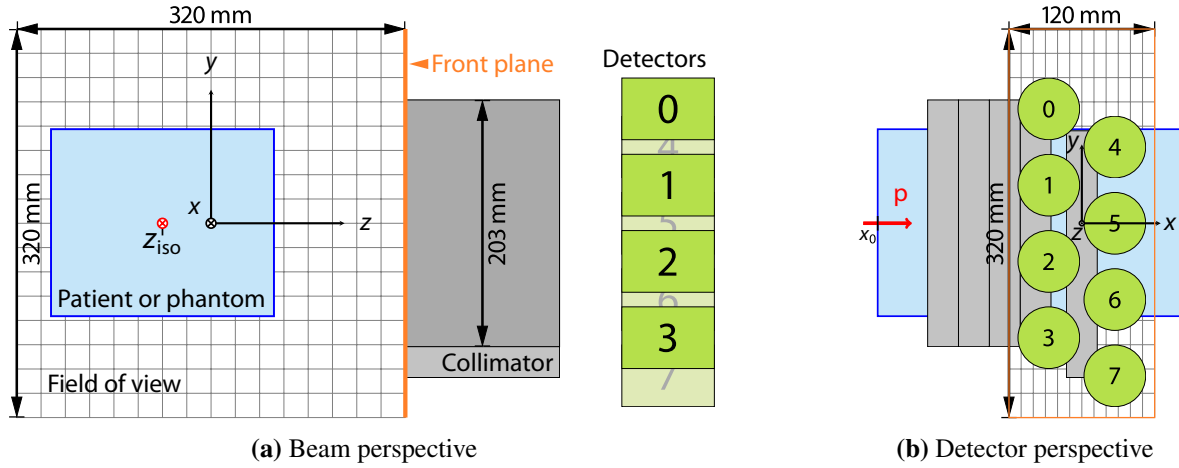


**Figure 3:** Sketch of the detector FOV from the perspective of the beam (a) and of an observer behind the detector (b). The collimator slabs (gray) and the eight detectors (green) are overlaid. A patient or phantom (blue) is shown as an example, that could be located anywhere within the FOV. The  $x$  axis is parallel to the beam axis (red), the  $y$  axis is parallel to the slit, and the  $z$  axis completes the right-handed triad, pointing towards the detectors. The  $x$  axis origin is on the center of the standalone collimator slab at a distance  $|x_0|$  from the upstream edge of the phantom or patient, whereas the  $y$  axis is centered on the proximal collimator block. The  $z$  axis origin is at 160 mm normal to the front plane (orange line) of the collimator and at a lateral distance  $|z_{iso}|$  of the central beam axis. The FOV covers a region of  $120 \times 320 \times 320 \text{ mm}^3$ .

they are the most abundant nuclear targets for prompt gamma-ray emission in human tissue (Verburg et al. 2012). Other elements have a minor contribution to the proton-induced signal, or none in the case of hydrogen.

### 3.3. Proton energy spectrum

The stopping of the pencil-beams within the patient or phantom is modeled using an extended version of gPMC (Jia et al. 2012; Qin et al. 2016), which is a CUDA GPU-accelerated Monte Carlo code specifically designed for proton therapy simulation. The simulations are performed on a Tesla K40 GPU accelerator (NVIDIA Corporation, Santa Clara, CA). The Monte Carlo beam model has been calibrated to match experimentally measured Bragg peaks following the method of Verburg et al. (2016). Through the use of the Monte Carlo method, geometries with complex tissue inhomogeneities, range straggling and strong multiple Coulomb scattering are modeled accurately.

To quantify the absolute proton range, we simulate several range error scenarios  $c$  in steps of 1 mm. The range of the protons in the GPU Monte Carlo simulation is altered by slightly changing the incident proton energy. We have automated the Monte Carlo simulation based on the treatment plan, the converted densities  $\hat{\rho}^{vt}$  and material compositions  $m^v$ . The output of the simulation is the deposited dose and the proton energy spectrum, i.e., the number of protons  $N_p^{c s v e}$  with kinetic energy  $e$  in each FOV voxel  $v$  for every pencil-beam spot  $s$  and range error scenario  $c$ .

**Table 3:** Nuclear reaction channels leading to abundant prompt gamma-ray emission in human tissue (Verburg et al. 2014), classified according to the oxygen and carbon target nuclei. The index  $l$  corresponds to that of table 1 and the energies of the prompt gamma-rays are given in MeV. Reactions which result in the emission of prompt gamma-rays with similar energies are clustered at the same index  $l$  as they cannot be resolved experimentally.

Index $l$	$\gamma$ energies / MeV	Reactions with $^{16}\text{O}$	Reactions with $^{12}\text{C}$
0	1.63	$^{16}\text{O}(p, x\gamma)^{14}\text{N}$	
1	2.00	$^{16}\text{O}(p, x\gamma)^{11}\text{C}$	$^{12}\text{C}(p, x\gamma)^{11}\text{C}$
	2.04	$^{16}\text{O}(p, x\gamma)^{15}\text{O}$	
2	2.31	$^{16}\text{O}(p, x\gamma)^{14}\text{N}$	
3	2.74	$^{16}\text{O}(p, p'\gamma)^{16}\text{O}$	
	2.79	$^{16}\text{O}(p, x\gamma)^{14}\text{N}$	
	2.80	$^{16}\text{O}(p, x\gamma)^{11}\text{C}$	$^{12}\text{C}(p, x\gamma)^{11}\text{C}$
	2.87	$^{16}\text{O}(p, x\gamma)^{10}\text{B}$	$^{12}\text{C}(p, x\gamma)^{10}\text{B}$
4	4.44	$^{16}\text{O}(p, x\gamma)^{12}\text{C}$	$^{12}\text{C}(p, p'\gamma)^{12}\text{C}$
	4.45	$^{16}\text{O}(p, x\gamma)^{11}\text{B}$	
5	5.24	$^{16}\text{O}(p, x\gamma)^{15}\text{O}$	
	5.27	$^{16}\text{O}(p, pp\gamma)^{15}\text{N}$	
	5.18	$^{16}\text{O}(p, x\gamma)^{15}\text{O}$	
	5.30	$^{16}\text{O}(p, pp\gamma)^{15}\text{N}$	
6	6.13	$^{16}\text{O}(p, p'\gamma)^{16}\text{O}$	
	6.18	$^{16}\text{O}(p, x\gamma)^{15}\text{O}$	

### 3.4. Prompt gamma-ray emission

The next step involves the calculation of the number of prompt gamma-rays with discrete energies  $l$  emitted along the beam path. We do not rely on a Monte Carlo simulation of the nuclear reactions and gamma-ray emissions; only experimentally determined cross sections are used. Besides the output data from the GPU Monte Carlo simulation  $N_p^{csve}$  and the target nuclei concentrations  $\hat{\rho}^{vt}$  from the CT scan, the differential cross sections  $\sigma^{elt}$  of every prompt gamma-ray transition  $l$  and target nucleus  $t$  are needed, which depend on the proton energy  $e$ . For the determination of the number of prompt gamma-rays  $N_\gamma^{csvlt}$  emitted along the beam path for each pencil-beam  $s$ , range error scenario  $c$ , voxel  $v$ , transition  $l$  and target nucleus  $t$ , the voxel-dependent proton energy distributions from the GPU Monte Carlo simulation are multiplied with the energy-dependent cross sections and target concentrations:

$$N_\gamma^{csvlt} = \sum_e N_p^{csve} \cdot \frac{\hat{\rho}^{vt} N_A}{A^t} \cdot 4\pi\sigma^{elt} \delta^v, \quad (4)$$

where  $\delta^v$  is the (mean) intersection length of the proton beam with voxel  $v$  (approximated by the FOV pixel size along  $x$ , i.e. 1 mm),  $A^t$  is the molar atomic mass of target element  $t$  and  $N_A$  is the Avogadro constant. The lines included in the model are described in table 1, and correspond to the nuclear reaction channels listed in table 3.

In addition, the proton continuum spectrum is considered, as it contains a significant fraction of the collected events. This continuum is in part due to gamma-rays from the

main discrete lines that do not deposit their full energy in the detectors. Another part, which contributes approximately to an equal extent, is the prompt gamma-ray quasi-continuum. These are emissions of unresolved gamma-rays  $\tilde{N}_\gamma^{csvlta}$  from unknown transitions  $l$  which are not resolvable in the measurement. This part is approximated by a linear combination of known lines with an effective cross section  $\psi^{eta}$  depending on the proton energy  $e$ , target  $t$ , and are associated with absorption processes  $a = 3, 4$  ( $\psi^{eta} = 0$  if  $a < 3$ ):

$$\tilde{N}_\gamma^{csvlta} = \sum_e u^l N_p^{csve} \cdot \frac{\hat{p}^v N_A}{A^t} \cdot 4\pi \psi^{eta} \delta^v, \quad (5)$$

where the constants  $u^l$  are normalized weights chosen such that the continuum gamma-ray emission energy spectrum is approximately constant up to 6 MeV.

The proton energy range that we model for the prompt gamma-ray emission within the detector FOV ranges from 0 to 150 MeV. The incident energy of the proton beam can be as high as the maximum energy of 230 MeV, because the energy of the protons is reduced to well below 150 MeV before they reach the FOV.

### 3.5. Gamma-ray attenuation

The calculation of the detection probability of the emitted gamma-rays is separated into two parts: a measurement-specific calculation of the gamma-ray attenuation based on the CT scan of the patient or phantom, and a model of the collimator-detector system that is the same for all measurements, which is discussed in the next section.

We define the transmission probability  $\tau^{v\theta\phi}$  for a gamma-ray with energy  $l$  traveling from FOV voxel  $v$  to the detector in the direction with angles  $(\theta, \phi)$  that reaches the detector front plane without undergoing any interaction, see figure 3a. It is modeled using a ray tracing algorithm (Amanatides et al. 1987) with the energy-dependent attenuation coefficients of the FOV voxels  $\mu^{v'l}$  calculated previously. The transmission probability is given by the sum along the path  $\ell'$  that connects voxel  $v$  with the crossing point on the front face plane, that is defined by  $\theta$  and  $\phi$ :

$$\tau^{v\theta\phi} = \exp\left(-\sum_{v'} \mu^{v'l} \delta\ell'\right), \quad (6)$$

where  $\delta\ell'$  is the intersection length of the path  $\ell'$  within the voxel  $v'$ .

### 3.6. Collimator-detector system response

The detection probability  $\eta^{p\theta\phi l da}$  of the collimator-scintillator system is determined using a Monte Carlo simulation of the electromagnetic interactions using the TOPAS Monte Carlo code (Perl et al. 2012) with the Geant4 10.04.p01 toolkit (Allison et al. 2016). The positions, dimensions and material compositions of all parts influencing the detection probability, i.e., the collimator and scintillation crystals, are included in the model. Photons with energies corresponding to the prompt gamma-ray lines  $l$  are simulated, originating from the front plane of the detection system, which is divided into pixels  $p$  as shown in figure 3b. The simulated

photons are emitted isotropically from all front plane positions and directions defined by angles  $\theta$  and  $\phi$ . Five types of events corresponding to different types of interactions  $a$  in the detectors  $d$  are counted. Events in which the whole initial photon energy is deposited in a single scintillation crystal ( $a = 0$ ) are counted as full energy detection events, (1) single and (2) double escape lines are simulated by counting the events where the deposited energy corresponds to the initial photon energy reduced by 511 keV, respectively 1.022 MeV. Additionally, any event with (3) a deposited energy between 1.4 MeV and 3.0 MeV or (4) a deposited energy higher than 3.0 MeV is recorded.

The total detection probability  $\xi^{vlda}$  for a gamma-ray of transition  $l$  originating from voxel  $v$ , not interacting until reaching the front plane and undergoing an absorption type  $a$  in detector  $d$  yields:

$$\xi^{vlda} = \sum_{\theta, \phi} \tau^{v\theta\phi} \cdot \eta^{p\theta\phi lda}, \quad (7)$$

where  $p$  is the pixel on the front plane that is intersected by the path from voxel  $v$  in the direction  $(\theta, \phi)$ .

### 3.7. Absolute range verification

The expected counts  $\zeta_{\gamma}^{csltda}$  according to the simulated model are calculated for every range error scenario  $c$ , pencil-beam spot  $s$  of the treatment plan, target nucleus  $t$ , prompt gamma-ray line  $l$ , interaction type  $a$  and detector  $d$ :

$$\zeta_{\gamma}^{csltda} = \sum_v \left( N_{\gamma}^{csvlt} + \tilde{N}_{\gamma}^{csvlta} \right) \cdot \xi^{vlda}, \quad (8)$$

and we sum over each detector row  $r$ :

$$\zeta_{\gamma}^{csltra} = \sum_{d=4r}^{4r+3} \zeta_{\gamma}^{csltda}. \quad (9)$$

The results of the independent simulations with discrete range error scenarios  $c$  are interpolated to get a continuous model of the counts ( $\zeta_{\gamma}^{csltra} \rightarrow \zeta_{\gamma}^{\varepsilon sltra}$ ) as a function of the absolute range error  $\varepsilon = (\check{c} - 8) \times (1 \text{ mm})$ , where  $\check{c}$  is the interpolated counterpart of  $c$ .

The absolute proton range of a pencil-beam spot  $s$  is determined by minimizing the least square residuals between the experimentally measured gamma-ray counts  $C_{\gamma}^{sltra}$  and the modeled ones  $\zeta_{\gamma}^{\varepsilon sltra}$ , leaving the range error scenario  $c$  and actual target concentrations  $\rho^{vt} = k^{vt} \hat{\rho}^{vt}$  as free parameters:

$$\operatorname{argmin}_{\varepsilon^s, k^{s0}, k^{s1}, \chi^{s3}} \left( \sum_{l,r,a} w^a \left\| \chi^{sa} \sum_t k^{st} \zeta_{\gamma}^{\varepsilon^s sltra} - C_{\gamma}^{sltra} \right\|_2^2 \right). \quad (10)$$

In total, for every spot, four parameters are fitted:  $\varepsilon^s, k^{s0}, k^{s1}, \chi^{s3}$ . The correction factors  $k^{v0}$  and  $k^{v1}$  of the target concentrations ( $\rho^{vt} = k^{vt} \hat{\rho}^{vt}$ ) are assumed to be a constant multiplier ( $k^{vt} \rightarrow k^{st}$ ) within the region of interest of the FOV of spot  $s$ .  $\chi^{sa}$  is a multiplication factor that is 1 if  $a < 3$  and is left as free parameter for the continuum absorption processes ( $\chi^{s3} = \chi^{s4}$ ). This multiplier allows to account for small concentrations of other nuclei that are not modeled

in the continuum emission, as well as small errors that are introduced by the fact that the gamma-ray attenuation in the patient cannot be exactly modeled for the continuum component.  $w^a$  is an empirical scaling constant which is 1 for  $a < 3$  and 0.1 otherwise, to equalize the absolute contribution of each absorption process to the least squares.

The measurement of the proton continuum  $C_\gamma^{slr3}$  and  $C_\gamma^{slr4}$  cannot be distinguished experimentally depending on  $l$ . The experimental value corresponds to the sum of all lines, and is redistributed among each line  $l$  according to the weights  $u^l$ , and is compared then to the values predicted by the simulation at absorption process  $a = 3$  or  $a = 4$  and line  $l$ .

The Levenberg–Marquardt algorithm was used to solve the optimization problem in equation (10). For the present detector geometry, the problem is convex and the optimization converges to the same global optimum independently of the initial values of the parameters.

### 3.8. Distal spot aggregation

Pencil-beam spots  $\tilde{s}$  that are delivered to the same lateral position of spot  $s$ , but to an adjacent energy layer with a proton range that differs by less than 10 mm, will be subject to almost the same range error scenario  $\epsilon^s \approx \epsilon^{\tilde{s}}$  and elemental concentration correction factors  $k^{st} \approx k^{\tilde{s}t}$ ,  $\chi^{sa} \approx \chi^{\tilde{s}a}$ . Instead of treating these spots as being fully independent, it is useful to determine their range error simultaneously to improve statistical precision. This is accomplished by simultaneously fitting the parameters for these spots, rather than by merging the histograms as done in the lateral direction (section §2.10). Hence, for each spot  $s$ , we optimize:

$$\operatorname{argmin}_{\epsilon^s, k^{s0}, k^{s1}, \chi^{s3}} \left( \sum_{s'} \sum_{l,r,a} w^a \left\| \chi^{sa} \sum_t k^{st} \zeta_\gamma^{\epsilon^s s' ltra} - C_\gamma^{s'lra} \right\|_2^2 \right), \quad (11)$$

where  $s'$  is a set of spots including the pencil-beam  $s$  and the aggregated ones  $\tilde{s}$ . When verifying the most distal energy layer, this normally results in only one spot  $\tilde{s}$  from the second most distal energy layer to be aggregated to the spot  $s$  under consideration.

### 3.9. Cross section optimization

The nuclear reaction cross sections  $\sigma^{elt}$  for the prompt gamma-ray production are the cornerstone of our model, which enable the absolute range verification based on fundamental physical principles. We previously published the cross sections that we use for  $^{16}\text{O}$  and  $^{12}\text{C}$  nuclei for a 90 degree angle between the incident beam and the detector (Verburg et al. 2014). These are based on a combination of our own measurements and previous literature referenced therein. Unlike other measurements that are typically performed at a few specific proton energies, we optimized the cross sections for the complete proton energy range from 0 to 150 MeV, which is required for range verification of beams stopping in matter. The range verification is not sensitive to small resonances in the cross sections because of the energy spread of the proton beam close to the end-of-range.

As is typical for cross section measurements, these are subject to some systematic errors due to issues such as the bias in the separation of the gamma-ray line from the background. Because our present system features new data acquisition algorithms and improved methods

to separate the gamma-ray lines from the background, we have re-optimized our previous cross sections  $\hat{\sigma}^{elt}$  by applying a small correction based on a reference measurement in water and in high-density polyethylene. Because of the improvements, we expect the re-optimized cross sections to have a smaller systematic error as compared to our previous optimization. By using the same system for the cross section optimization and the range verification, this re-optimization is also effectively a calibration that removes the effect of the system-specific systematic bias.

To obtain the optimized cross sections  $\sigma^{elt}$ , we minimize the discrepancy between the measured gamma-ray counts  $C_\gamma^{slra}$  and the values predicted by the model  $\zeta_\gamma^{csltra}$  for the nominal case  $c = 8$  (0 mm range error) and each target  $t = 0, 1$ , line  $l$  and proton energy  $e$ :

$$\operatorname{argmin}_{\sigma^{elt}} \left( \sum_{a=0}^2 \sum_{s,r} \left\| k^{st} \zeta_\gamma^{8sltra} - C_\gamma^{slra} \right\|_2^2 + \lambda \left\| \sigma^{elt} - \hat{\sigma}^{elt} \right\|_2^2 \right), \quad (12)$$

where

$$\zeta_\gamma^{8sltra} = \sum_{d=4r}^{4r+3} \sum_{e,v} N_p^{8sve} \cdot \frac{\rho^v N_A}{A_t} \cdot 4\pi \delta^v \left( \sigma^{elt} + u^l \cdot \psi^{eta} \right) \cdot \xi^{vlda} \quad (13)$$

and  $\lambda$  is an empirical damping factor. The first term is the least squares optimization between the model and the measurement, while the second one is a Tikhonov regularization term to penalize large differences between the reference cross sections  $\hat{\sigma}^{elt}$  and the optimized ones  $\sigma^{elt}$ . Note that, in this calibration experiment,  $k^{st}$  is fixed as the target composition is well known.

Likewise, for the effective cross sections  $\psi^{eta}$  that describe the unresolved continuum, we optimize for  $a = 3$  and  $a = 4$ :

$$\operatorname{argmin}_{\psi^{eta}} \left( \sum_{s,l,r} \left\| k^{st} \zeta_\gamma^{8sltra} - C_\gamma^{slra} \right\|_2^2 \right). \quad (14)$$

## 4. Experimental setups

### 4.1. Cross section optimization

The measurements for the cross section optimization were performed during the delivery of a single high-dose spot ( $3 \times 10^{10}$  protons) along the central beam axis consecutively to 19 energy layers to either a water phantom or to a solid block of polyethylene. The phantom was mounted on a linear stage on breadboard for accurate positioning. We estimate the positioning uncertainty in depth to be  $\pm 0.5$  mm. The proton ranges were between 10 cm and 15 cm water equivalent, corresponding to incident energies of 116 MeV to 145 MeV. In this setup, the detector FOV (see figure 3) was centered at a depth of  $-x_0 = 124$  mm in the phantom and the distance between the isocenter and the front plane of the collimator was 150 mm ( $z_{iso} = 10$  mm), including an air gap of 100 mm.

**Table 4:** Characteristics of the treatment plan designed for delivering 0.9 Gy dose uniformly to a  $5.3 \times 10 \times 10 \text{ cm}^3$  target volume in water with a beam current of 2 nA, see figures 4 and 5, divided in eight iso-energy layers. The reported proton range  $R_{80}$  is the physical distance from the phantom front face.

Layer	Proton energy MeV	Range $R_{80}$ mm	# spots	# protons $\times 10^9$	Protons / spot $\times 10^9$ (mean)	Dose to target Gy (mean)
0	176	210	203	24.1	0.12	0.25
1	173	203	217	29.1	0.13	0.32
2	168	194	199	12.8	0.06	0.13
3	164	186	180	8.2	0.05	0.08
4	160	178	180	7.7	0.04	0.06
5	156	171	167	6.3	0.04	0.04
6	152	163	127	4.0	0.03	0.02
7	148	155	137	5.7	0.04	0.02
Total			1410	97.9	0.07	0.91

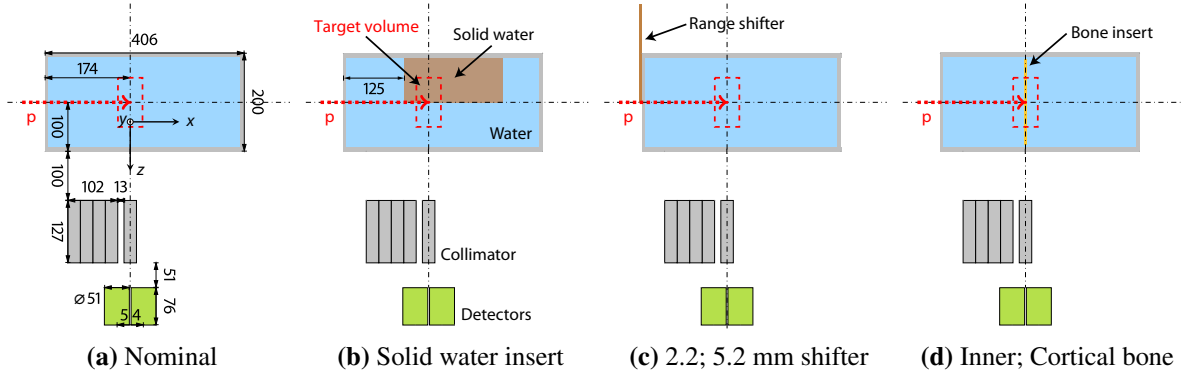


**Figure 4:** Schematic of the experimental setups to assess the range verification performance (top view, dimensions are in mm). Protons (red arrow) irradiate the water phantom (blue: water, light gray: walls), where  $x_0 = -174 \text{ mm}$  and  $z_{\text{iso}} = -40 \text{ mm}$ . The FOV coordinate system is defined in figure 3. The black dash-dotted lines intersect at isocenter. The dashed red rectangle is the target volume ( $5.3 \times 10 \times 10 \text{ cm}^3$ ). The prompt gamma-rays are collimated (gray) and measured with scintillation detectors (green). (a) Reference case in water with no range error. (b) Solid water block (brown) covering half of the field. (c) 2.2 mm or 5.2 mm water equivalent range shifter (brown) covering half of the field. (d) 5 mm thick slab (orange) of inner or SB3 cortical bone inserted in the middle of the field.

#### 4.2. Absolute range verification

To test the range verification with a clinically realistic pencil-beam field, we designed a treatment plan to deliver a uniform dose of 0.9 Gy to a  $5.3 \times 10 \times 10 \text{ cm}^3$  target in water, as shown in figure 4a. The isocenter was located centrally in the target and the distance between isocenter and the collimator front face was 200 mm ( $z_{\text{iso}} = -40 \text{ mm}$ ). There was an air gap of 100 mm between the collimator and the phantom, which would also be realistic when the system is used clinically. The FOV center was at a depth of  $-x_0 = 174 \text{ mm}$  in the phantom, see figure 3.

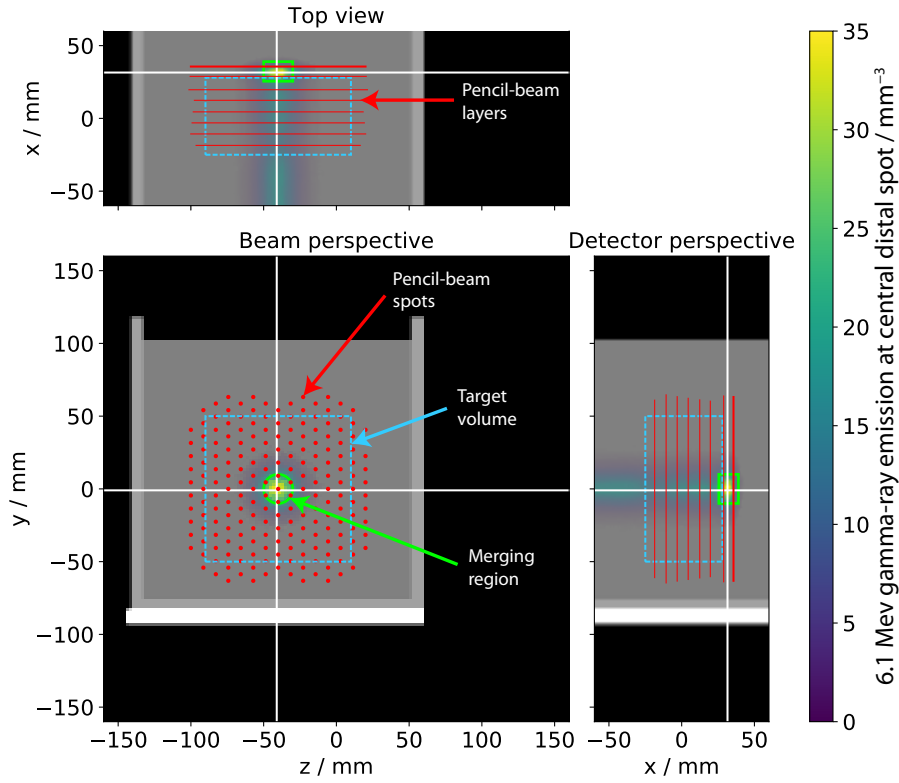


**Figure 5:** Visualization of the planning images and pencil-beam positions in the treatment plan, superimposed with the modeled 6.1 MeV prompt gamma-ray emission density  $N_{\gamma}^{c=8,s=101,v,t=6,t=0} / (1 \times 2 \times 2 \text{ mm}^3)$  for the central spot of the distal layer, see equation (4). Relative to the field of view (figure 3), the top view is at slice  $y = 0$  mm, the beam perspective is at slice  $x = 31$  mm, and the detector perspective is at slice  $z = -40$  mm (white cross-hair lines). The phantom setup corresponds to figure 4a, placed at  $x_0 = -174$  mm and  $z_{\text{iso}} = -40$  mm. The pencil-beam spot scanning pattern is overlaid in the beam's eye view, as red spots. The green cylinder (circle or rectangle in the projections) indicates a 10 mm merging radius and a 10 mm depth, enclosing spots from the two distal energy layers, as explained in sections §2.10 and 3.8. The dashed blue rectangles represent the target region of the treatment plan. The red lines mark the nominal ranges  $R_{80}$  of the pencil-beam energy layers (table 4).

The treatment plan was created using our in-house Astroid treatment planning system (Kooy et al. 2010). The dose was delivered to the target volume with a total of 1410 pencil-beams in eight energy layers, as described in table 4. The uniform dose region of the proton pencil-beams extends between 15 cm and 20.3 cm depth. The lateral distance between two neighboring pencil-beam spots in the distal energy layer is approximately 9 mm and the separation between consecutive energy layers is about 8 mm. We used the standard clinical CT conversion, assuming the phantom to consist of soft tissue. This means that the model has no prior knowledge of the actual elemental composition, which is left as free parameter  $k^{st}$  to be fitted simultaneously to the absolute range error  $\epsilon^s$ , see equation (11).

Figure 5 shows the pencil-beam scanning treatment plan and the prompt gamma-ray emission for one of the pencil-beam spots. We also show the merging region that defines the area in which we aggregate the measurement data for range verification, as discussed

in sections §2.10 and 3.8. Altogether, including the lateral merging, the merging region corresponding to spot  $s$  can be visualized as a cylinder of 10 mm radius and 10 mm depth, enclosing typically a total of 14 pencil-beams, i.e. 7 from each layer.

The range verification performance was further assessed by introducing different inhomogeneities in this setup, as shown in figure 4:

- Setup 4a is the reference case where no range error is expected.
- In setup 4b, a solid water block (Gammex RMI, Middleton WI) is inserted in half of the water phantom at a depth of 125 mm. This setup is devoted to test the capability of the prototype to accurately detect the absolute range independently of the elemental composition of the irradiated tissue. Solid water has a stopping power close to that of water (1.02 ratio), but a by-mass elemental composition of 67% C, 20% O and 8% H (Hünemohr et al. 2014), very different from that of water (89% O, 11% H). A shift of 1.7 mm of the end-of-range is expected for the pencil-beams of the distal energy layer going through the solid water.
- Setup 4c includes a range shifter placed in front of the water phantom and covering half of the field. We used range shifters with a water equivalent thickness of 2.2 and 5.2 mm.
- In setup 4d, a bone equivalent slab with a thickness of 5 mm of inner or SB3 cortical bone (Gammex) is inserted into the water phantom, centered at a depth of 174 mm. The expected shifts of the end-of-range are 0.5 mm for inner bone and 3.0 mm for cortical bone.

The expected range shifts created by the Gammex materials were determined based on proton stopping power measurements that we performed by measuring the shift in the Bragg peak position in water when the materials are placed in the beam path. The stopping powers that we measured are consistent with the measurements by Saito et al. (2017) and Hünemohr et al. (2014).

## 5. Results

### 5.1. Energy- and time-resolved histograms

An example of the acquired energy- and time-resolved prompt gamma-ray histogram and the separation into the different components (2.9) is presented in figure 6. This histogram was acquired during the cross section calibration experiment (section §4.1), in which a high dose was delivered. It shows the excellent performance of the detectors and the data acquisition system at a beam current of 2 nA. During the delivery of the distal layer, the count rate in each detector was on the order of  $10^6$  events per second. Even under these conditions, an energy resolution of 1.3% full width at half maximum was obtained at 6.1 MeV, allowing the gamma-ray lines to be clearly resolved. A robust separation of the continuum and resolved components can be observed. The background constitutes approximately half of the detected gamma-rays, including sources such as the proton treatment head, phantom, couch, walls and floor of the treatment room. There is also some production of neutron-induced gamma-rays in the collimator, but most of these are re-absorbed internally.

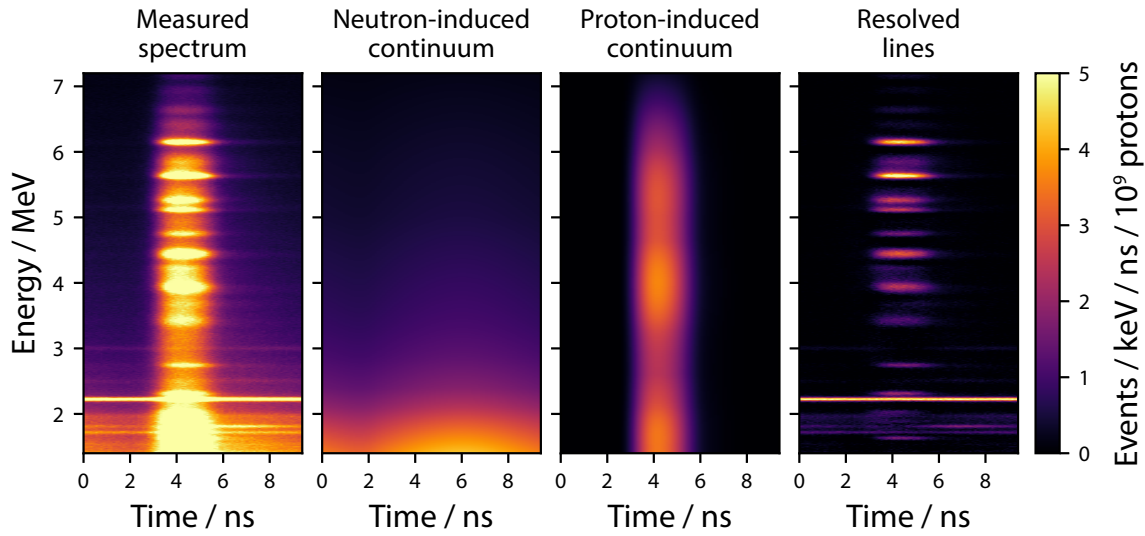


**Figure 6:** From left to right: measured 2D spectrum of the energy deposit over trigger time with respect to the cyclotron radiofrequency; the neutron- and proton-continuum background estimated by our algorithm; resolved neutron-induced and proton-induced lines. This measurement was performed during the irradiation of a water phantom with 2 nA beam current. These spectra were measured by detector row  $r = 1$  during the cross section optimization experiment (section §3.9), where a high dose was delivered. Piled-up or coincident events have been excluded.

### 5.2. Cross section optimization

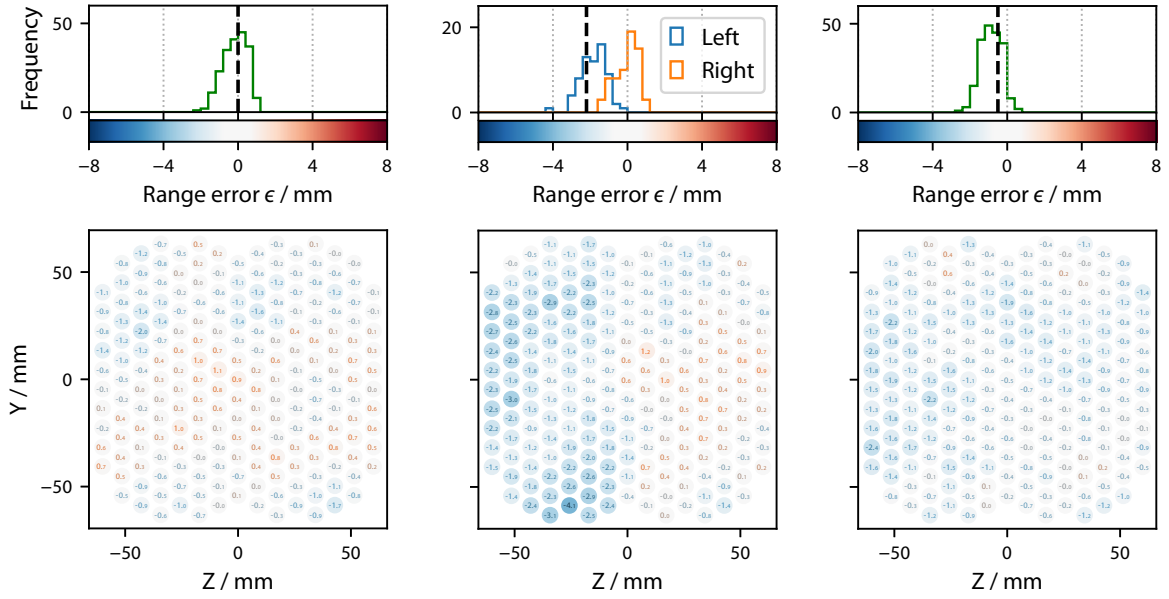
The consistency of the re-optimized cross sections was verified by calculating the relative deviation  $\Delta^{lt} = \langle 1 - \sigma^{elt} / \hat{\sigma}^{elt} \rangle$  between the optimized and our previous cross sections (Verburg et al. 2014), averaged over the proton energy range from 0 MeV to 150 MeV. For the more prominent prompt gamma-ray lines, the differences are  $\Delta^{40} = 17\%$ ,  $\Delta^{41} = 5\%$ , and  $\Delta^{61} = 12\%$ .

### 5.3. Absolute range verification

In figure 7, the absolute range verification is shown for the experiments in which a dose of 0.9 Gy was delivered to a target in different phantom setups. These results were obtained for each spot of the most distal energy layer, using a cylindrical merging region of 10 mm radius and 10 mm depth, as shown in figure 5. Note that the range errors are not calculated with respect to a previous measurement, but with respect to the value predicted by the simulated model with only the planning CT as prior information.

The experimental setups correspond to figure 4: featuring no range shifter (figure 4a), a solid water insert in half of the field (figure 4b), a range shifter covering half of the field upstream of the water phantom (figure 4c) and a bone insert slab within the phantom covering the full field (figure 4d).

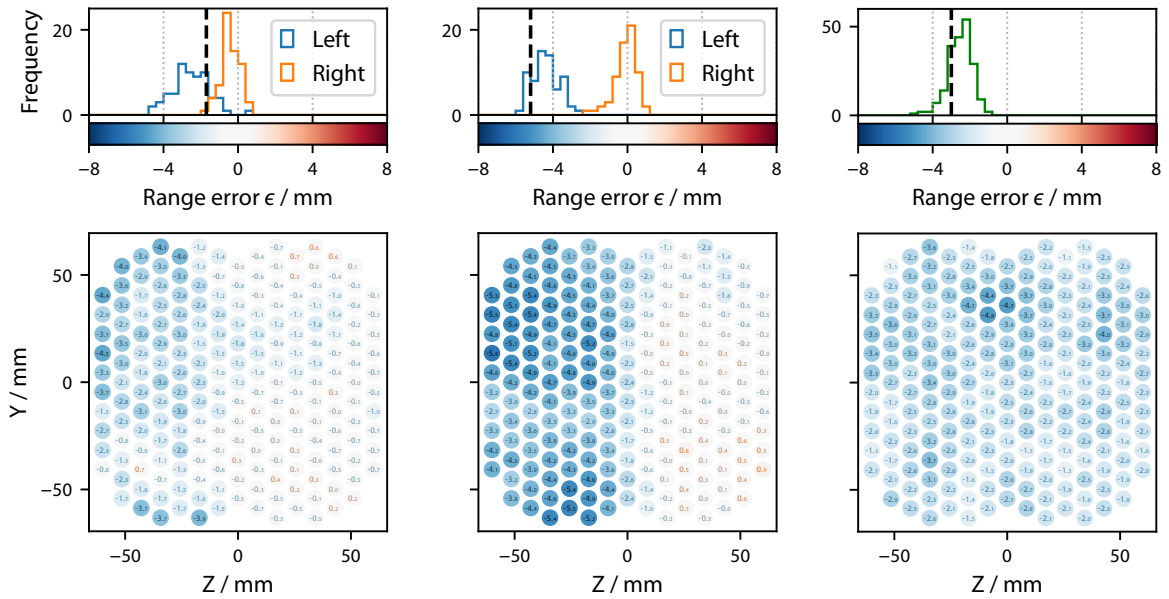
In figure 8, the determined oxygen and carbon concentrations are shown for two of the experiments: the nominal case without range shifter (figure 4a) and the setup with a solid water



(a) Nominal case, figure 4a.

(c) 2.2 mm shifter on left, figure 4c.

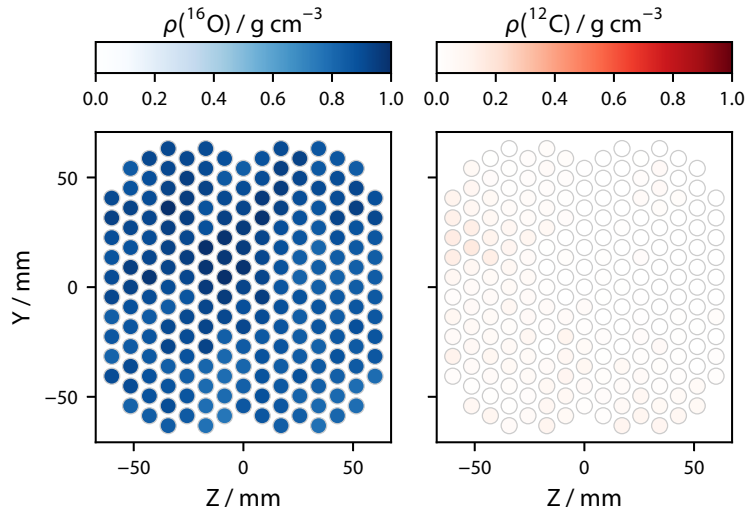
(e) Inner bone, figure 4d.



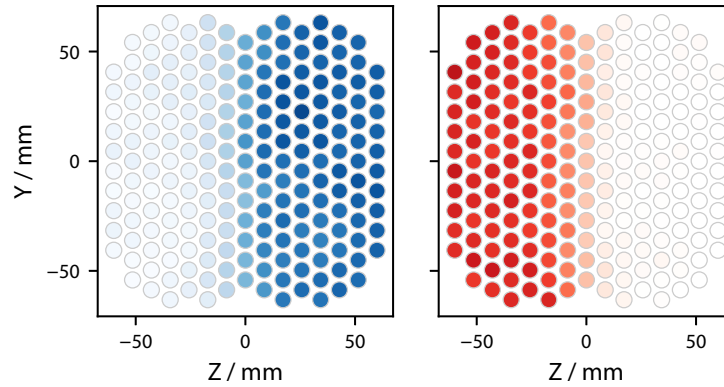
(b) Solid water insert on left, figure 4b. (d) 5.2 mm shifter on left, figure 4c.

(f) Cortical bone, figure 4d.

**Figure 7:** Range verification of the distal layer of a proton pencil-beam field delivering 0.9 Gy to a  $5.3 \times 10 \times 10 \text{ cm}^3$  region. The Y and Z axis correspond to the y and z –  $z_{\text{iso}}$  axes of figure 3. The proton range error  $\epsilon^s$  with respect to the model prediction is annotated within the colored circles. Shown are the experiments without range shifter (a), with a solid water insert in the left half of the field (b), with a 2.2 mm (c) and 5.2 mm (d) range shifter covering the left half of the field, and with the inner (e) and SB3 cortical (f) bone inserts. Each spot contains information from a cylindrical merging region of 10 mm depth and 10 mm radius (figure 5). The histograms show the range errors with a bin width of 0.4 mm, in which a dashed black vertical line marks the theoretically introduced range shift. Where relevant, the histograms are shown separately for the left ( $Z < -20$  mm) and right ( $Z > 20$  mm) parts of the field.



(a) Nominal case with liquid water, see figure 4a.



(b) Solid water insert on the left half of the field, see figure 4b.

**Figure 8:** Elemental composition determination for the same pencil-beam field as in figure 7. The oxygen and carbon concentrations by mass  $\rho^{st}$  are shown in the left and right columns. The reference case (a) is compared with the solid water insert in the left half of the field (b). Each spot contains information from a cylindrical merging region of 10 mm depth and 10 mm radius.

insert in half of the field (figure 4b). The differences in elemental composition in the different parts of the field can be clearly identified.

To determine the mean accuracy and the mean statistical precision of the range verification, we repeated all of the above experiments 12 times. The results are listed in table 5. Averaging all experiments, the mean systematic deviation in the determined range was 0.5 mm. The mean statistical precision, determined by calculating the standard deviation of the repeat measurements, was 1.1 mm at a 95% confidence level ( $2\sigma$ ) for the chosen merging radius of 10 mm and 10 mm depth. For the case of the solid water insert (figure 7b), we obtain a larger statistical uncertainty (1.9 mm) in the left part of the field. This is in accordance with the lower prompt gamma-ray yield of carbon with respect to oxygen targets (Verburg et al. 2014; Pinto

**Table 5:** Determined range error and elemental concentrations for the pencil-beams irradiating the different setups, averaged over the distal energy layer. The mean absolute range error and the mean statistical precision ( $\pm 2\sigma$ ) are listed. The range error  $\varepsilon$  refers to the difference between the measured range of the pencil-beams and the model prediction based on the treatment plan. Where relevant, the results are given separately for the left part of the field ( $Z < -20$  mm) and the right part ( $Z > 20$  mm). The statistics were calculated based on 12 repeated measurements.

Setup	Range error $\varepsilon$ / mm		$\rho(^{16}\text{O})$ / $\text{g cm}^{-3}$		$\rho(^{12}\text{C})$ / $\text{g cm}^{-3}$	
	Left	Right	Left	Right	Left	Right
4a - Nominal	$-0.2 \pm 1.0$		$0.88 \pm 0.09$		$0.05 \pm 0.06$	
Expected	0.0		0.89		0.00	
4b - Solid water	$-2.4 \pm 1.9$	$-0.5 \pm 1.0$	$0.17 \pm 0.05$	$0.88 \pm 0.10$	$0.76 \pm 0.08$	$0.03 \pm 0.05$
Expected	-1.7	0.0	0.20	0.89	0.67	0.00
4c - 2.2 mm shifter	$-1.9 \pm 1.1$	$-0.4 \pm 0.9$	$0.90 \pm 0.10$	$0.88 \pm 0.07$	$0.07 \pm 0.08$	$0.03 \pm 0.05$
Expected	-2.2	0.0	0.89	0.89	0.00	0.00
4c - 5.2 mm shifter	$-4.4 \pm 1.1$	$-0.4 \pm 0.9$	$0.88 \pm 0.09$	$0.88 \pm 0.07$	$0.07 \pm 0.08$	$0.02 \pm 0.05$
Expected	-5.2	0.0	0.89	0.89	0.00	0.00
4d - Inner bone	$-0.8 \pm 1.0$		$0.87 \pm 0.10$		$0.09 \pm 0.08$	
Expected	-0.5		0.89		0.00	
4d - Cortical bone	$-2.3 \pm 1.0$		$0.85 \pm 0.09$		$0.10 \pm 0.08$	
Expected	-3.0		0.89		0.00	

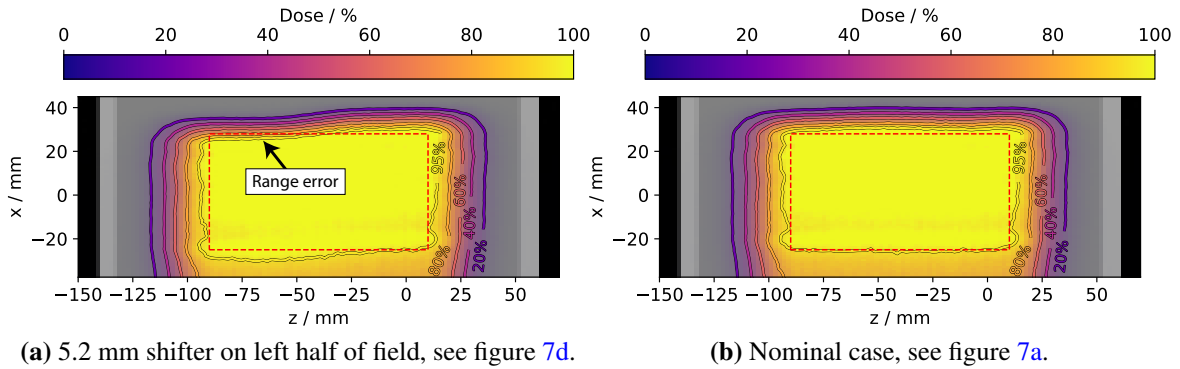


**Figure 9:** Planning images superimposed with the reconstructed proton dose based on the measurements of figure 7. The pencil-beams are simulated with the GPU based on the measured proton range. Axes are in mm and correspond to the FOV definition (figure 3). The red dashed rectangle shows the target region of  $5.3 \text{ cm} \times 10 \text{ cm}$  covered uniformly with 0.9 Gy. The image corresponds to slice  $y = 0 \text{ mm}$ . Isodose lines at 95%, 80%, 60%, 40% and 20% levels of the target dose are shown.

et al. 2015). The fitted elemental compositions are in agreement with the expected values in all cases.

We also recalculated the dose distributions based on the range verification results. In figure 9, the central slice  $y = 0 \text{ mm}$  of the dose distribution in the water phantom is shown. The setup with a 5.2 mm range shifter on the left part of the field (figure 7d) is compared to the reference case (figure 7a). The underdosage in the distal part of the target volume (red dashed rectangle) and the overdosage in the proximal region, that are introduced by the range shift, can be observed.

## 6. Discussion

Compared to our forerunner pre-clinical prototype with a single detector (Verburg et al. 2014), we have further developed and scaled up our prompt gamma-ray spectroscopy technology to achieve millimeter accuracy in proton range verification at a clinical beam current and dose. Even under these challenging conditions, our system is uniquely able to perform energy- and time-resolved prompt gamma-ray measurements that are normalized to absolute units, which facilitates a direct comparison with nuclear reaction models. The statistical precision achieved with this prototype outperforms previously published results from other prompt gamma-ray imaging systems at clinical beam currents and doses, mainly because of the higher detector throughput and efficiency.

Prompt gamma-ray spectroscopy has the advantage of incorporating an energy- and time-resolved event analysis in addition to the spatial collimation. The range verification algorithm is therefore able to reconstruct the proton range and the elemental composition of the target tissue simultaneously. This reduces the bias in the retrieved proton range by minimizing the uncertainty in the tissue composition, which can be different from the estimation based on the planning CT scan due to conversion ambiguity. A potential future improvement is to incorporate dual-energy CT for characterization of the elemental composition (Wohlfahrt et al. 2017). This would improve the accuracy of our model and it may be used to set constraints on the elemental concentrations  $\rho^{vt}$ .

Our method considers many different nuclear reaction channels, which yields redundant information for a reliable range verification. The model enables the prediction of the absolute proton range with a bias below 1 millimeter only based on the planning CT, the measured gamma-rays and fundamental physical principles. The simulation is based on established Monte Carlo methods, tabulated nuclear cross sections, and an empirical calibration of the unresolved proton continuum. This direct physical basis overcomes one of the main limitations of range verification using positron emission tomography, where biological washout effects need to be considered, which are difficult to model (Knopf et al. 2011).

The performance of our system is enhanced by the design of the collimator, which is set up in such a way that the FOV is focused on the distal edge of the Bragg peak, where the emitted prompt gamma-rays have a stronger correlation with the range of the beam than in the entrance path. The slit opening is chosen as a compromise between systematic uncertainties and statistical precision: a narrower collimator would increase the spatial resolution but impair the collected statistics in detector row  $r = 0$ . The open slit configuration for the distal detector row  $r = 1$ , as previously shown by Verburg et al. 2015, maximizes the number of collected events at the end-of-range. In an actual patient, where the beam entrance surface might not be flat and the tissue is not homogeneous, the proton ranges of the spots from the same energy layer will not be at the same depth with respect to the collimator. Hence, having two detector rows at different depths will be beneficial to enclose most of the proton stopping points within the FOV.

The range errors that we introduced in this work were range undershoots. In the case of a range overshoot, the statistical precision will be higher because of more gamma-rays

reaching the detectors. Also, as expected from the prompt gamma-ray yields, the statistical precision is higher in matter with a high  $^{16}\text{O}$  concentration as compared to matter with a high  $^{12}\text{C}$  concentration. This is advantageous for clinical range verification. The oxygen fraction in a variety of tumor samples has been shown to range between 57% and 78% (Maughan et al. 1998). Brain tissue and soft tissue, which are often critical organs, are also rich in oxygen.

The aggregation of prompt gamma-ray measurements from proton pencil-beams within a 10 mm lateral merging radius and a 10 mm depth is what we believe constitutes a good trade-off between resolution and statistical precision. The data that we used for the range verification of each distal spot correspond to the delivery of about  $1.6 \times 10^9$  protons and a mean accumulated dose to the target volume of 1.6 cGy. In the case of single-field optimization of the dose delivery, as was used in the experiments in this work, the large majority of the protons stop very close the distal end of the target. Therefore, the verification of the range of the distal proton energy layers is of main importance. Multi-field optimized treatment plans created with robust optimization also deliver most dose to the distal layers, because the delivery of additional dose outside the target volume is possible there to account for range uncertainty. When prompt gamma-ray spectroscopy allows for a significant reduction of the range uncertainty, intensity-modulated treatment plans may be designed with higher doses being delivered to parts of the more proximal energy layers. In this situation, it will likely be advantageous to use a spatially varying merging region to account for the local differences in the delivered number of protons.

The prompt gamma-ray spectroscopy method is able to estimate the real composition, as well as the magnitude of the range error, even if the delivered pencil-beam ranges are quite different from the treatment plan. Several potential range errors are simulated and the most likely one according to the match with the measurements is determined. It is however possible that complex differences occur between the treatment planning and the delivery, for example, if the heterogeneities in the beam path are very different as compared to the plan. In this case, significant discrepancies between the model and the measurement data would be observable, which might be more difficult to interpret as only a range error. This would serve as an indication that the positioning of the patient has to be checked and that re-planning may be necessary. When adaptive workflows based on a daily cone-beam CT become more commonplace, this would be less of an issue.

For a smooth integration of our prototype in the clinical workflow during the first patient study, we are developing a six-axis positioning robot and a laser alignment system. Our rotating detector frame will be mounted on these actuators as shown in figure 10, which will enable a fast, accurate and reproducible detector alignment with respect to the patient using several alignment lasers. The robot itself will stand on a mobile platform.

The reconstructed proton range and dose will be superimposed on the patient CT to assess for significant range deviations with respect to the treatment plan, as shown in figure 9a. As emphasized by Verburg et al. (2014), the absolute range can be determined without prior knowledge of the tissue composition already for the first treatment fraction, and further relative range shifts can be detected for later fractions with high precision.

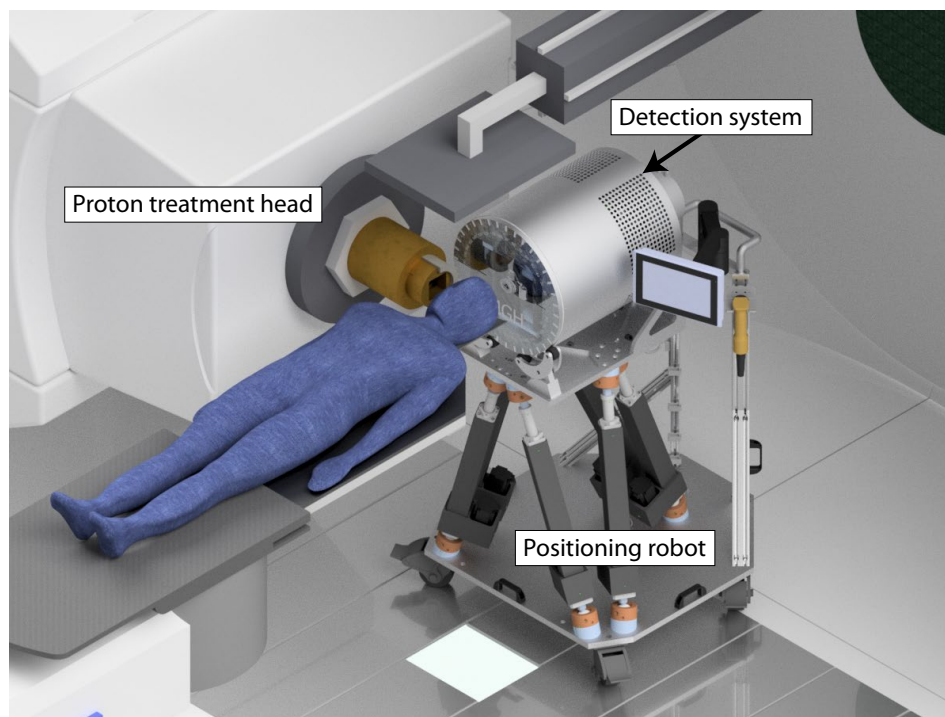


**Figure 10:** Illustration of the gantry, proton treatment head, patient, top x-ray flat panel and our prototype range verification system. The detector frame can rotate according to the gantry angle, and is mounted on a positioning robot, consisting of six actuators. The robot stands on a platform on wheels that is moved into the treatment room. The adult phantom was modeled by [Chuang Yu Lun](#).

Once the robustness and accuracy of the prototype is demonstrated during actual treatments, the prompt gamma-ray spectroscopy system could promote the correction of range errors in upcoming treatment fractions with re-planning, thus improving the quality of treatment and, potentially, the outcome. On a longer term, we envision real-time adaptation of the range, the reduction of range margins, and novel treatment plan designs that take advantage of the sharp distal gradient of the Bragg peak to maximize the sparing of organs-at-risks that surround the target volume.

## 7. Conclusions

A full-scale clinical prototype system for proton range verification using prompt gamma-ray spectroscopy was tested with phantoms at the pencil-beam scanning gantry treatment room of the Francis H. Burr Proton Therapy Center. The developed electronics and calibration methods performed well at a clinical beam current of 2 nA incident on the phantoms. A detailed model of prompt gamma-ray emission and system response was developed, that enables the reconstruction of both the proton range and the elemental composition of the irradiated matter based on the measurements.

The absolute range was determined for each pencil-beam spot of the distal energy layer with a mean statistical precision of 1.1 mm at a 95% confidence level and a mean absolute deviation of 0.5 mm, for a delivered dose of 0.9 Gy, and by aggregating data from pencil-beams in a merging cylinder of 10 mm radius and 10 mm depth. Range errors that we introduced were detected accurately even in the presence of large differences in the elemental composition with respect to the assumptions based on the planning CT scan.

Our results show for the first time that proton range verification with 1 millimeter precision is achievable in phantoms under clinically realistic conditions. An experiment with a ground-truth anthropomorphic head phantom (Wohlfahrt et al. 2018) is planned as the final validation prior to our upcoming clinical study, where we will test our prototype during the treatment of patients with brain tumors.

### Acknowledgments

We thank Arthur Brown, Pablo Botas, Ethan Cascio, Bob Brett, Tom Madden, Georgios Patoulidis and the staff of the proton therapy facility for their excellent support. This work was supported in part by the Federal Share of program income earned by Massachusetts General Hospital on C06-CA059267, Proton Therapy Research and Treatment Center, and by the National Cancer Institute grant U19 CA021239-35. The Tesla K40 GPU was donated by the NVIDIA Corporation.

### References

- [1] F. Albertini, E. B. Hug, and A. J. Lomax. Is it necessary to plan with safety margins for actively scanned proton therapy? *Phys. Med. Biol.* 56.14 (2011), p. 4399. URL: <http://dx.doi.org/10.1088/0031-9155/56/14/011>.
- [2] S. Aldawood et al. Development of a Compton camera for prompt-gamma medical imaging. *Radiat. Phys. Chem.* 140.Suppl C (2017), pp. 190–197. URL: <https://doi.org/10.1016/j.radphyschem.2017.01.024>.
- [3] J. Allison et al. Recent developments in Geant4. *Nucl. Instrum. Methods Phys. Res., Sect. A* 835 (2016), pp. 186–225. URL: <https://doi.org/10.1016/j.nima.2016.06.125>.
- [4] J. Amanatides and A. Woo. A fast voxel traversal algorithm for ray tracing. In: *Eurographics*. Vol. 87. 3. 1987, pp. 3–10. URL: <https://diglib.org/handle/10.2312/egtp19871000?show=full>.
- [5] P. Andreo. On the clinical spatial resolution achievable with protons and heavier charged particle radiotherapy beams. *Phys. Med. Biol.* 54.11 (2009), N205. URL: <http://dx.doi.org/10.1088/0031-9155/54/11/N01>.

- [6] V. Bécares and J. Blázquez. Detector Dead Time Determination and Optimal Counting Rate for a Detector Near a Spallation Source or a Subcritical Multiplying System. *Sci Techn Nucl Inst* 2012.240693 (2012), pp. 1–7. URL: <http://dx.doi.org/10.1155/2012/240693>.
- [7] M. Berger et al. XCOM: Photon Cross Section Database, NIST Standard Reference Database 8 (XGAM). *NIST* (2010). URL: <http://www.nist.gov/pml/data/xcom>.
- [8] R. Capote et al. RIPL - Reference Input Parameter Library for Calculation of Nuclear Reactions and Nuclear Data Evaluations. *Nucl. Data Sheets* 110.12 (2009), pp. 3107–3214. URL: <https://doi.org/10.1016/j.nds.2009.10.004>.
- [9] E. Draeger et al. 3D prompt gamma imaging for proton beam range verification. *Phys. Med. Biol.* 63.3 (2018), p. 035019. URL: <https://doi.org/10.1088/1361-6560/aaa203>.
- [10] C. Golnik et al. Range assessment in particle therapy based on prompt  $\gamma$ -ray timing measurements. *Phys. Med. Biol.* 59.18 (2014), p. 5399. URL: <http://dx.doi.org/10.1088/0031-9155/59/18/5399>.
- [11] F. Hueso-González et al. Prompt gamma rays detected with a BGO block Compton camera reveal range deviations of therapeutic proton beams. *IEEE Trans Radiat Plasma Med Sci* 1.1 (2017), pp. 76–86. URL: <http://dx.doi.org/10.1109/TNS.2016.2622162>.
- [12] F. Hueso-González et al. First test of the prompt gamma ray timing method with heterogeneous targets at a clinical proton therapy facility. *Phys. Med. Biol.* 60.16 (2015), p. 6247. URL: <http://dx.doi.org/10.1088/0031-9155/60/16/6247>.
- [13] F. Hueso-González et al. Test of Compton camera components for prompt gamma imaging at the ELBE bremsstrahlung beam. *J. Instrum.* 9.05 (2014), P05002. URL: <http://dx.doi.org/10.1088/1748-0221/9/05/P05002>.
- [14] N. Hünemohr et al. Experimental verification of ion stopping power prediction from dual energy CT data in tissue surrogates. *Phys. Med. Biol.* 59.1 (2014), p. 83. URL: <https://doi.org/10.1088/0031-9155/59/1/83>.
- [15] X. Jia et al. GPU-based fast Monte Carlo dose calculation for proton therapy. *Phys. Med. Biol.* 57.23 (2012), p. 7783. URL: <https://doi.org/10.1088/0031-9155/57/23/7783>.
- [16] Y. Jongen and F. Stichelbaut. Verification of the proton beam position in the patient by the prompt gamma rays emission. In: *PTCOG Conf Rec.* 2003, p. 16. URL: [https://www.ptcog.ch/archive/steering\\_committee\\_docs/ptcog39-2003/2003\\_PTCOG\\_39\\_Abstracts.pdf](https://www.ptcog.ch/archive/steering_committee_docs/ptcog39-2003/2003_PTCOG_39_Abstracts.pdf).
- [17] A.-C. Knopf and A. Lomax. In vivo proton range verification: a review. *Phys. Med. Biol.* 58.15 (2013), R131. URL: <http://dx.doi.org/10.1088/0031-9155/58/15/R131>.

- [18] A.-C. Knopf et al. Accuracy of Proton Beam Range Verification Using Post-Treatment Positron Emission Tomography/Computed Tomography as Function of Treatment Site. *Int. J. Radiat. Oncol. Biol. Phys.* 79.1 (2011), pp. 297–304. URL: <https://doi.org/10.1016/j.ijrobp.2010.02.017>.
- [19] H. M. Kooy et al. A Case Study in Proton Pencil-Beam Scanning Delivery. *Int. J. Radiat. Oncol. Biol. Phys.* 76.2 (2010), pp. 624–630. URL: <https://doi.org/10.1016/j.ijrobp.2009.06.065>.
- [20] J. Krimmer et al. A cost-effective monitoring technique in particle therapy via uncollimated prompt gamma peak integration. *Appl. Phys. Lett.* 110.15 (2017), p. 154102. URL: <https://doi.org/10.1063/1.4980103>.
- [21] J. Krimmer et al. Prompt-gamma monitoring in hadrontherapy: A review. *Radiat Ima Tech Appl* 878 (2018), pp. 58–73. URL: <https://doi.org/10.1016/j.nima.2017.07.063>.
- [22] R. L. Maughan et al. The elemental composition of tumors: Kerma data for neutrons. *Med. Phys.* 24.8 (1998), pp. 1241–1244. URL: <http://dx.doi.org/10.1118/1.598144>.
- [23] G. Pausch et al. Scintillator-based high-throughput fast timing spectroscopy for real-time range verification in particle therapy. *Trans. Nucl. Sci.* 63.2 (2016), pp. 664–672. URL: <http://dx.doi.org/10.1109/TNS.2016.2527822>.
- [24] J. Perl et al. TOPAS: an innovative proton Monte Carlo platform for research and clinical applications. *Med. Phys.* 39.11 (2012), pp. 6818–6837. URL: <https://doi.org/10.1118/1.4758060>.
- [25] J. Petzoldt et al. Characterization of the microbunch time structure of proton pencil beams at a clinical treatment facility. *Phys. Med. Biol.* 61.6 (2016), p. 2432. URL: <http://dx.doi.org/10.1088/0031-9155/61/6/2432>.
- [26] M. Pinto et al. Absolute prompt-gamma yield measurements for ion beam therapy monitoring. *Phys. Med. Biol.* 60.2 (2015), p. 565. URL: <http://dx.doi.org/10.1088/0031-9155/60/2/565>.
- [27] M. Pinto et al. Design optimisation of a TOF-based collimated camera prototype for online hadrontherapy monitoring. *Phys. Med. Biol.* 59.24 (2014), p. 7653. URL: <http://dx.doi.org/10.1088/0031-9155/59/24/7653>.
- [28] N. Qin et al. Recent developments and comprehensive evaluations of a GPU-based Monte Carlo package for proton therapy. *Phys. Med. Biol.* 61.20 (2016), p. 7347. URL: <https://doi.org/10.1088/0031-9155/61/20/7347>.
- [29] C. Richter et al. First clinical application of a prompt gamma based in vivo proton range verification system. *Radioth Oncol* 118.2 (2016), pp. 232–237. URL: <http://dx.doi.org/10.1016/j.radonc.2016.01.004>.
- [30] H. Rohling et al. Requirements for a Compton camera for in-vivo range verification of proton therapy. *Phys. Med. Biol.* 62.7 (2017), p. 2795. URL: <https://doi.org/10.1088/1361-6560/aa6068>.

- [31] C. Ryan et al. SNIP, a statistics-sensitive background treatment for the quantitative analysis of PIXE spectra in geoscience applications. *Nucl Instrum Methods Phys Res B* 34.3 (1988), pp. 396–402. URL: [http://dx.doi.org/10.1016/0168-583X\(88\)90063-8](http://dx.doi.org/10.1016/0168-583X(88)90063-8).
- [32] M. Saito and S. Sagara. Simplified derivation of stopping power ratio in the human body from dual-energy CT data. *Med. Phys.* 44.8 (2017), pp. 4179–4187. URL: <https://doi.org/10.1002/mp.12386>.
- [33] W. Schneider, T. Bortfeld, and W. Schlegel. Correlation between CT numbers and tissue parameters needed for Monte Carlo simulations of clinical dose distributions. *Phys. Med. Biol.* 45.2 (2000), p. 459. URL: <https://doi.org/10.1088/0031-9155/45/2/314>.
- [34] A. Schumann et al. From prompt gamma distribution to dose: a novel approach combining an evolutionary algorithm and filtering based on Gaussian-powerlaw convolutions. *Phys Med Biol* 61.19 (2016), p. 6919. URL: <https://doi.org/10.1088/0031-9155/61/19/6919>.
- [35] K. S. Seo, C. H. Kim, and J. W. Kim. Comparison of Titanium Hydride (TiH<sub>2</sub>) and Paraffin as Neutron Moderator Material in a Prompt Gamma Scanning System. *J Korean Phys Soc* 48.4 (2006), p. 855. URL: <http://www.jkps.or.kr/journal/view.html?uid=7726&vmd=Full>.
- [36] J. Smeets et al. Prompt gamma imaging with a slit camera for real-time range control in proton therapy. *Phys. Med. Biol.* 57.11 (2012), p. 3371. URL: <http://dx.doi.org/10.1088/0031-9155/57/11/3371>.
- [37] P. Solevi et al. Performance of MACACO Compton telescope for ion-beam therapy monitoring: first test with proton beams. *Phys. Med. Biol.* 61.14 (2016), p. 5149. URL: <http://dx.doi.org/10.1088/0031-9155/61/14/5149>.
- [38] J. Unkelbach, T. C. Y. Chan, and T. Bortfeld. Accounting for range uncertainties in the optimization of intensity modulated proton therapy. *Phys. Med. Biol.* 52.10 (2007), p. 2755. URL: <https://doi.org/10.1088/0031-9155/52/10/009>.
- [39] J. M. Verburg and J. Seco. Proton range verification through prompt gamma-ray spectroscopy. *Phys. Med. Biol.* 59.23 (2014), p. 7089. URL: <http://dx.doi.org/10.1088/0031-9155/59/23/7089>.
- [40] J. M. Verburg, H. A. Shih, and J. Seco. Simulation of prompt gamma-ray emission during proton radiotherapy. *Phys. Med. Biol.* 57.17 (2012), p. 5459. URL: <http://dx.doi.org/10.1088/0031-9155/57/17/5459>.
- [41] J. M. Verburg, M. Testa, and J. Seco. Range verification of passively scattered proton beams using prompt gamma-ray detection. *Phys. Med. Biol.* 60.3 (2015), p. 1019. URL: <http://dx.doi.org/10.1088/0031-9155/60/3/1019>.
- [42] J. M. Verburg et al. Automated Monte Carlo Simulation of Proton Therapy Treatment Plans. *Technology in Cancer Research & Treatment* 15.6 (2016), NP35–NP46. URL: <https://doi.org/10.1177/1533034615614139>.

- [43] J. M. Verburg et al. Energy- and time-resolved detection of prompt gamma-rays for proton range verification. *Phys. Med. Biol.* 58.20 (2013), p. L37. URL: <http://dx.doi.org/10.1088/0031-9155/58/20/L37>.
- [44] P. Wohlfahrt et al. Dual-energy CT based proton range prediction in head and pelvic tumor patients. *Radioth Oncol* 125.3 (2017), pp. 526–533. URL: <https://doi.org/10.1016/j.radonc.2017.09.042>.
- [45] P. Wohlfahrt et al. Evaluation of Stopping-Power Prediction by Dual- and Single-Energy Computed Tomography in an Anthropomorphic Ground-Truth Phantom. *Int J Radiat Oncol Biol Phys* 100.1 (2018), pp. 244–253. URL: <https://doi.org/10.1016/j.ijrobp.2017.09.025>.
- [46] Y. Xie et al. Prompt Gamma Imaging for In Vivo Range Verification of Pencil Beam Scanning Proton Therapy. *Int. J. Radiat. Oncol. Biol. Phys.* 99.1 (2017), pp. 210–218. URL: <http://dx.doi.org/10.1016/j.ijrobp.2017.04.027>.